Heliyon 9 (2023) e20540

Contents lists available at ScienceDirect

Heliyon

journal homepage: www.cell.com/heliyon

Research article

Characterizing infection risk in a restaurant environment due to airborne diseases using discrete droplet dispersion simulations

Rahul Bale [a,b,*], ChungGang Li [c], Hajime Fukudome [d], Saori Yumino [e], Akiyoshi Iida [f], Makoto Tsubokura [a,b]

[a] RIKEN Center for Computational Sciences, Kobe, Japan
[b] Graduate School of System Informatics, Kobe University, Kobe, Japan
[c] Department of Mechanical Engineering, National Cheng Kung University, Taiwan
[d] Numerical Flow Design, Tokyo, Japan
[e] Kajima Corporation, Tokyo, Japan
[f] Department of Mechanical Engineering, Toyohashi University of Technology, Toyohashi, Japan

ARTICLE INFO

Keywords:
Airborne diseases
Droplet dispersion simulations
Probability of infection

ABSTRACT

The use of masks as a measure to control the spread of respiratory viruses has been widely acknowledged. However, there are instances where wearing a mask is not possible, making these environments potential vectors for virus transmission. Such environments can contain multiple sources of infection and are challenging to characterize in terms of infection risk. To address this issue, we have developed a methodology to investigate the role of ventilation in reducing the infection risk in such environments. We use a restaurant setting as a representative scenario to demonstrate the methodology. Using implicit large eddy simulations along with discrete droplet dispersion modeling we investigate the impact of ventilation and physical distance on the spread of respiratory viruses and the risk of infection. Our findings show that operating ventilation systems, such as mechanical mixing and increasing physical distance between subjects, can significantly reduce the average room infection risk and number of newly infected subjects. However, this observation is subject to the transmissibility of the airborne viruses. In the case of a highly transmissible virus, the use of mechanical mixing may be inconsequential when compared to only fresh air ventilation. These findings provide valuable insights into the mitigation of infection risk in situations where the use of masks is not possible.

1. Introduction

The spread of diseases through the release of virus-containing sputum droplets into the air can pose a significant threat to public health. This has been demonstrated in recent decades with the emergence of several highly infectious diseases such as Severe Acute Respiratory Syndrome (SARS), H1N1 influenza, and the current pandemic of Coronavirus Disease 2019 (COVID-19) [1,2]. COVID-19 has quickly spread worldwide, leading to hundreds of millions of infections and deaths. Additionally, the indirect impact of the pandemic, such as loss of livelihood and economic shrinkage, is challenging to quantify. The evidence suggests that SARS-CoV-2, the virus responsible for COVID-19, can be transmitted through respiratory droplets, direct person-to-person contact, and contact

* Corresponding author at: RIKEN Center for Computational Sciences, Kobe, Japan, and Kobe Univeristy, Kobe, Japan.
E-mail address: rahul.bale@riken.jp (R. Bale).

https://doi.org/10.1016/j.heliyon.2023.e20540
Received 25 August 2023; Received in revised form 28 September 2023; Accepted 28 September 2023

Available online 4 October 2023

with contaminated surfaces (known as fomite transmission). Airborne transmission is likely a major factor in the rapid spread of COVID-19, turning it into a global pandemic [3,4]. While direct person-to-person and fomite transmission can be controlled through wearing masks and proper hygiene practices, preventing airborne transmission is more challenging. Controlling and reducing airborne transmission is crucial in preventing the spread of communicable diseases and protecting public health.

There have been several previous studies examining the relationship between indoor ventilation and the transmission of airborne particle aerosols in different setups, such as large rooms [5,6], medical clinics [7], medical centres [8], conference rooms [9], and supermarkets [10]. Additionally, research has focused on the transmission characteristics and infection potential of droplets exhaled by people in transportation environments like aircraft cabins [8], train carriages [11] and buses [12]. The primary focus of most of these studies is characterizing the flow within the indoor environment generated by expiratory events on the distance and dispersion of the droplets. However, there is little to no focus on characterizing the droplet/pollutant data into in probability of infection risk information. Furthermore, in studies consisting of multiple human model subjects, there has been no work on investigating the risk of infection considering multiple sources of infection within a given setup. Possible reasons for this could be the difficulty in characterizing the infection risk due to multiple sources of infection; considering multiple sources of infection may necessitate as many numerical simulations or experiments. Notwithstanding these difficulties, quantifying infection risk considering as many possible scenarios/sources of infection within a given setup can provide statistically more generalizable information about the infection risk of the setup under consideration.

The use of masks has been widely accepted as an effective way to reduce airborne transmission of diseases [13,5,14]. As a result, policymakers worldwide have encouraged the use of masks in all indoor and outdoor public spaces, with varying levels of success. In most social scenarios considered in prior studies, human subjects can be expected to use face masks to mitigate the spread of respiratory droplets [9,10,8,11,12]. This is possibly due to the assumption that all human subjects within the setup other than the source of infection use face masks. While mask usage can help to contain the spread of airborne pollutants, there are social situations where the use of masks is impossible. Indoor spaces like restaurants, cafeterias, bars, and pubs with live performances may become vectors for airborne disease transmission due to the inability or impracticality of wearing masks in these spaces. Therefore, it is necessary to assess the infection risk in these types of spaces in order to develop effective mitigation strategies. These spaces are also perfect candidates where it is reasonable to assume that all or any of the occupants could be sources of infection. Consequently, it is necessary to treat all the occupants as sources of infection while studying such spaces. Furthermore, as discussed in the preceding paragraph, a framework for quantification of infection risk when multiple sources of infection are present in a setup is also necessary.

This work aims to provide a methodology to characterize the infection risk in setups involving more than one source of infection and adopt it for the investigation of infection risk and potential mitigation strategies in a restaurant setting using numerical simulations of droplet dispersion. We use a fully compressible Navier-Stokes solver that takes into account the evaporated phase of droplets and its impact on droplet evaporation. We employ a discrete Lagrangian droplet model to model droplet transport and evaporation. This model is connected to the flow equations to establish a weak two-way coupling between the droplets and the flow.

2. Methods

2.1. Governing equations

The present work adopts a fully compressible Navier-Stokes solver coupled with discrete droplet modeling for droplet dispersion simulations. A Lagrangian-Eulerian approach is employed for the solver, wherein the equations of motion of the carrier/background fluid are solved in an Eulerian reference frame. At the same time, the droplets are modelled as discrete Lagrangian particles. The governing equations for the conservation of mass, momentum, energy and species concentration in compact notation can be written as

$$\frac{\partial \rho}{\partial t} + \frac{\partial \rho u_i}{\partial x_j} = 0$$

$$\frac{\partial u_i}{\partial t} + \frac{\partial \rho u_i u_j}{\partial x_j} = -\frac{\partial P}{\partial x_i} + \frac{\partial A_{ij}}{\partial x_j} + (\rho - \rho_0) g_i$$

$$\frac{\partial \rho e}{\partial t} + \frac{\partial (\rho e + P) u_j}{\partial x_j} = \frac{\partial A_{ij} u_i}{\partial x_j} - \frac{\partial q_j}{\partial x_j} + (\rho - \rho_0) g_i u_i$$

$$\frac{\partial \rho Y_k}{\partial t} + \frac{\partial \rho u_j Y_k}{\partial x_j} = \frac{\partial}{\partial x_j}\left(\rho D_k \frac{\partial Y_k}{\partial x_j}\right) + S_{\rho Y_k}$$

Here, density, velocity, pressure and total specific energy of the flow are represented by ρ, u_i, P and e, respectively. The transport equation for the k^{th} species is considered to model the transport of evaporated vapour phase of the liquid droplets. Y_k represents the mass fraction and D_k is the diffusivity of the k^{th} species. Although the species transport equation is presented in a general form, in the present work, only species transport equation of the vapour is considered. The components of the velocity vector $\mathbf{u}$ along the orthogonal directions $1, 2, 3$ are u_1, u_2, u_3, respectively. The total specific energy is given by $\rho e = \frac{P}{\gamma - 1} + \rho \frac{1}{2} u_i u_i$, where γ is the ratio of the gas specific heat capacities. A_{ij} is the viscous stress tensor, $\mathbf{q} = -\lambda \nabla T$, is the heat flux where T and λ represent temperature and thermal diffusivity, respectively. The density and pressure are constrained by the state equation $P = \rho R T$, in which R is the gas constant and T is the temperature. The source term in the momentum and energy conservation equations comprises contributions due to buoyancy force. In contrast, the source term in the species transport equation $S_{\rho Y_k}$ arises due to the two-way coupling between

the droplet model and the species equation of droplet vapour. ρ_0 in the buoyancy body force term represents the reference or far-field ambient density, and $\mathbf{g}$ is the acceleration due to gravity (e.g. $\mathbf{g} = (0, 0, -9.81) m/s^2$).

The contribution to the source terms in the mass, momentum, energy and species mass fraction conservation equations arises predominantly from two factors: the buoyancy term and the droplet evaporation process. Given that the sputum droplet's movement is primarily dictated by the airflow generated within the oral cavity, and not the other way around, the impact of droplet motion on the momentum of the carrying fluid is likely minimal. Consequently, this aspect is disregarded.

The total mass of sputum expelled via droplets smaller than 100 μm approximates to 10^{-8} kg. These droplets, upon expulsion from the mouth, are dispersed across a volume of roughly 2 cm^2. The corresponding mass of air within this specified region is around 8×10^{-6} g. Assuming an instantaneous and complete evaporation of all droplets within this volume, the mass contribution to the carrier gas would merely amount to approximately 0.125%. Thus, the mass contribution of droplets (with diameters $d_d < 100$ μm) to the carrier gas via evaporation is virtually negligible.

Regarding droplets with diameters $d_d > 100$ μm, their evaporation time scale is significantly longer compared to the time scale of velocity alterations due to gravity. Consequently, larger droplets swiftly descend and accumulate on the ground prior to evaporation, rendering their overall contribution to the region of interest limited.

The rate of droplet evaporation is strongly affected by the partial pressure at the droplet's surface, which in turn relies on the local mass fraction of the droplet's vapour phase. Minor alterations in this local mass fraction, brought on by droplet evaporation, can instigate changes in the evaporation rate, thereby establishing a feedback loop. As such, the effect of droplet evaporation is incorporated into the model via the source term in the species transport equation for the droplet's vapour phase.

2.2. Droplet model

The liquid sputum droplets are modelled as Lagrangian particles in the simulation framework. The Lagrangian droplets are coupled with the fluid flow with a one-way coupling, and the species transport equation of the evaporated phase of the sputum with a two-way coupling. The conditions of the ambient air influence droplet transport and evaporation, but the flow field is not affected by the droplets except for the species of the vapour phase of the liquid droplet. Such a framework may be referred to as a weak two-way coupling framework. The droplet transport is modelled by updating its position and velocity through the following equations

$$\frac{d\mathbf{x}_d}{dt} = \mathbf{u}_d,$$
$$\frac{d\mathbf{u}_d}{dt} = \frac{3C_D}{4d_d}\frac{\rho}{\rho_d}\left(\mathbf{u} - \mathbf{u}_d\right)\left|\mathbf{u} - \mathbf{u}_d\right| + \mathbf{g},$$

where $\mathbf{x}_d$, $\mathbf{u}_d$, d_d and ρ_d are the position, velocity, diameter and liquid density of each droplet, respectively. The drag coefficient C_D which is a function of Reynolds number Re_d is given by

$$C_d = \begin{cases} \frac{24}{Re_d}\left(1 + 1/6 Re_d^{2/3}\right) & Re_d < 1000, \\ 0.424 & Re_d > 1000, \end{cases}$$

in which the droplet Reynolds number is given by $Re_d = \rho(\mathbf{u} - \mathbf{u}_d)d_d/\mu$. The droplet diameter is updated by tracking the rate of change of droplet mass m_d and droplet temperature T_d

$$\frac{dT_d}{dt} = \frac{Nu}{3Pr}\frac{c_p}{c_l}\frac{f_1}{\tau_d}\left(T - T_d\right) + \frac{1}{m_d}\left(\frac{dm_d}{dt}\right)\frac{L_V}{c_{p,d}}$$
$$\frac{dm_d}{dt} = -\frac{m_d}{\tau_d}\left(\frac{Sh}{3Sc}\right)\ln\left(1 + B_M\right)$$

The convective heat transfer with the ambient air and the evaporative heat loss are accounted for to update the droplet temperature. B_m is the mass transfer number which considers the influence of the local vapour fraction on the droplet evaporation. The changes to the local vapour fraction due to the relative velocity between the droplet and fluid enhance the evaporation, which is considered through the Sherwood number Sh. Here, L_V is the latent heat of evaporation at the droplet temperature, respectively. c_p and c_l are the specific heat at a constant pressure of the ambient air, and the specific heat capacity of the liquid droplet, τ_d is the response time of the droplet, and Sc is the Schmidt number. A unit Lewis number is assumed under which $Sc = Pr$, where Pr is the Prandtl number. The source term to the species transport equation due to evaporation of the droplet is given by $S_{\rho Y} = -\frac{1}{\Delta V}\sum_n \frac{dm_d}{dt}$., where the summation is carried out over n droplets in one computational cell of volume ΔV. Further details of the various terms involved in the droplet model can be found in the work of Bale et al. [15,16] The liquid sputum is assumed to be composed on water and viral particles. Under such an assumption, total evaporation of the volatile component of a droplet leads to aerosolization. Therefore, a limiting value is necessary for the droplet diameter below which the droplet evaporation is ignored. The size of coronaviruses is in the range of 60 to 140 nm [17], therefore, for the limiting value of the droplet diameter we choose 1 μm. The chosen limit for the diameter allows for up to several hundred virions in one droplet post aerosolization. Lowering the limiter diameter will have little to no influence on the droplet transport behaviour while increasing the value may affect the droplet transport. Therefore, 1 μm is a reasonable value for the aerosolization of a droplet.

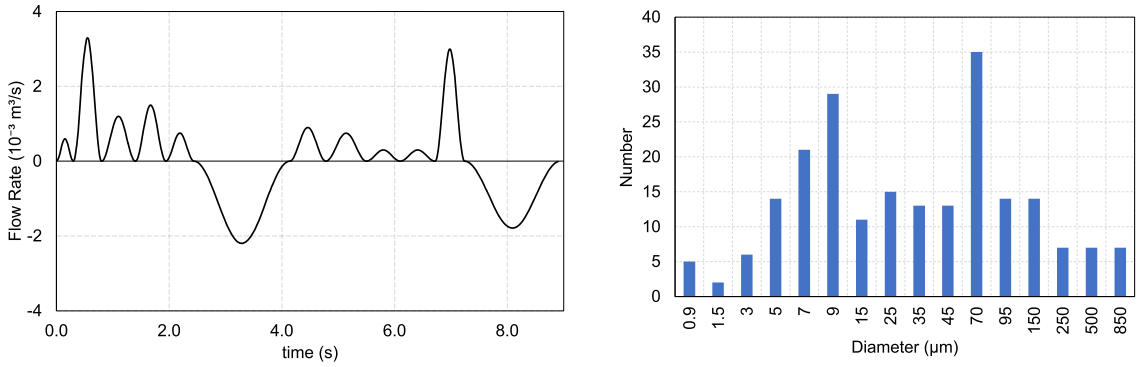

Fig. 1. a) The flow rate generated when counting from 1 to 10 interspersed with two inhalation phases [23]. b) Droplet size distribution.

In our model, the interaction of the droplet with the wall is governed by a set of critical conditions, particularly focusing on the wall-normal velocity and the critical Weber number of the droplet. During the initial phase of this interaction, we first ascertain if the droplet's wall-normal velocity is greater than the rate of change of the droplet's wall normal distance. This step is essential to determine whether the droplet possesses enough kinetic energy to either attach or rebound from the wall.

Following this, we evaluate the droplet's critical Weber number. The Weber number, $We = \rho_d u_d^{\perp} d_d/(\sigma_d)$, is a dimensionless quantity that provides a measure of the relative importance of the fluid's inertia compared to its surface tension. Here, $u_d^{\perp}, d_d$ and σ_d are the wall normal velocity, diameter, and surface tension of the droplet, respectively. In our model, if the droplet's critical Weber number is less than $2630La^{-0.183}$, where $La = \sigma_d \rho_d d_d/\mu_d$ is the droplet Laplace number, the droplet is assumed to attach to the wall. In the expression for Laplace number, μ_d is the viscosity of the droplet fluid. Conversely, if the droplet's critical Weber number exceeds this threshold, the droplet is considered to rebound, signifying that its inertia overcomes the surface tension, preventing attachment.

2.3. Speaking and droplet model

The modelling of droplet dispersion during speech requires three primary input parameters, a) the size distribution and the number of droplets ejected during the speech, b) the rate of exhalation as a function of time ejected during the speech, and c) the area of the mouth opening during speech. The data on the droplet size distribution reported in the literature for speaking varies significantly [18–21]. The droplet concentration (#/L), a proxy for droplet number, for speaking reported by Duiguid, Loudon and Roberts, and Chao et al. are 3.72, 223.25 and 150.8 [22,18,19], respectively. The difference in the reported droplet size distribution is also as disparate as the data on droplet concentration. The peak of the droplet size distribution reported by Loudon and Roberts [18], Duguid [22], and Xie et al. [21] correspond to the diameters 6 μm, 12 μm and 50 μm, respectively. Given the significant variation in the droplet size distribution reported in the literature, in the present work, we selectively combine the droplet size distribution reported by Duguid [22] and Loudon & Roberts [18]. The distribution adopted in this work essentially follows that of Duiguid [22] with a modification to the number count corresponding to 70 μm diameter by doubling it to include the effect of the peak of Loudon & Roberts distribution, which occurs around 70 μm. In our model, we have accounted for scenarios where individuals may be speaking loudly, particularly in environments such as restaurants. Here, the ambient noise from background music or lively conversations often prompts individuals to raise their speaking volume, especially under the influence of alcohol. This elevated volume can lead to an increase in the emission of larger droplets. Furthermore, the droplet distribution reported in the literature is based on the speaking patterns in the English language. In the experiments of evaluating droplet distribution during speech in the Japanese language, we found that the number and count of droplets between 20 μm to 70 μm were higher than those reported in literature. In order to account for the modelling of elevated volume of speech and the variation in droplet size distribution depending on the language, we increased the proportion of the intermediate droplet sizes reported in literature. The droplet count for diameters less than 20 μm are increased by a factor of 1.5, droplets larger than 70 μm are increased by a factor of 7, and the remaining droplets are increased by a factor that linearly increases from 1.5 to 7 as the diameter is increased from 20 μm to 70 μm. The droplet diameter distribution for loud speaking adopted for the numerical simulations in this work is shown in Fig. 1a.

The speaking flow adopted in this work is based on the experimental measurement of Gupta et al. [23] when subjects count from 1 to 10 in the English language. Based on the peak flow rate and duration of each utterance reported by Gupta et al. [23], the flow generated during the speech is represented as a sinusoidal model. The flowrate generated when counting from 1 to 10 is modelled as $\dot{q} = A_i \sin^2(\pi t/T_i)$, where A_i is the amplitude and T_i is the period of the i^{th} utterance or inhalation. Between the words 'five' and 'six', an inhalation phase is included that balances the total mass of fluid exhaled, counting from 'one' to '5'. Similarly, another inhalation phase is added after the word 'ten', balancing the mass of fluid exhaled when counting from 'six' to 'ten'. The speaking model counting from 'one' to 'ten', along with the two inhalation phases, constitutes one cycle of the model, which is repeated during the simulation. Assuming a loud speaking scenario, the amplitude of the flow rate of each utterance reported in [23] is increased by 50%, which is presented in Fig. 1b. We choose a circular surface that is 6 cm^2 in the area to model the mouth opening during

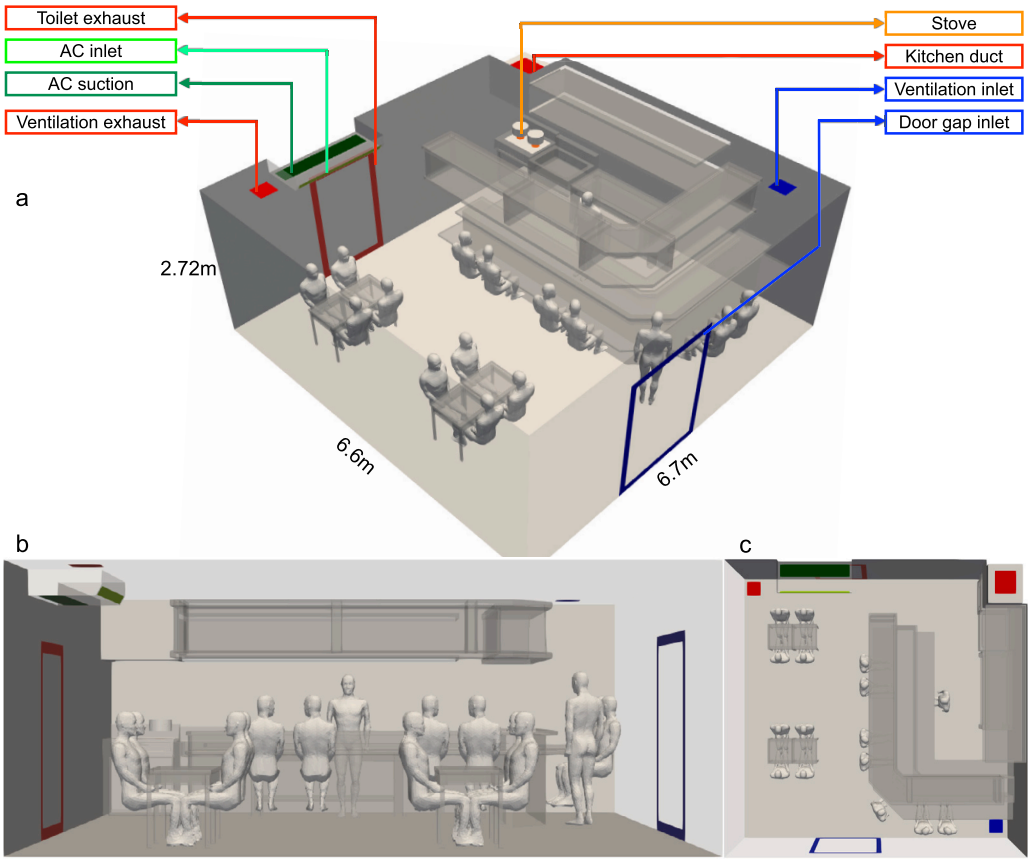

Fig. 2. The geometry of the restaurant setup in three different views (a) iso, (b) side and (c) top view.

speech. The droplets are injected in front of the circular mouth model within a distance of local mesh spacing. The injection timing corresponds to the time instants of the peak velocity of each utterance.

2.4. Restaurant setup

We consider a restaurant setup representative of a typical medium-sized Japanese izakaya. The restaurant houses an open kitchen with a seating arrangement for customers on a kitchen counter and a separate area for table seating. The setup is housed in a rectangular room measuring $6.7 \times 6.6 \times 2.3$ m^3. The seating arrangement consists of two tables, each of which can seat four subjects, and an L-shaped kitchen counter with space for six subjects to sit and one to stand. In this setup, we consider all the seating/standing spaces to be occupied by human subjects and an additional human subject to model the cooking staff in the kitchen area, resulting in 16 subjects. An isometric, side and top view of the restaurant geometry is presented in Fig. 2a, Fig. 2b and Fig. 2c, respectively. The subjects seated at the tables are assumed to be speaking to the subjects across the table. Therefore, they are modelled to be facing forward. The seated subjects at the kitchen counter are assumed to talk to their immediate neighbour on the left or right. To that effect, the head of the human geometry is modelled to turn 45^o sideways towards the immediate neighbour. The two standing subjects, namely the customer at the counter and the kitchen staff, are modelled to face forward while speaking.

The room's air-circulation system comprises fresh air ventilation, air conditioning, and kitchen exhaust systems. Fresh air is supplied to the room through the ventilation inlet at the bottom right corner of the ceiling as viewed from the top in Fig. 2c). About 81.48% of the exhaust removal from the room is carried out in the ventilation exhaust, while the balance of stale air removal is achieved through the toilet exhaust. The ventilation inlet, exhaust, and toilet exhaust make up the ventilation system. An air conditioning (AC) unit is included to model the room's cooling, consisting of an inlet that supplies cool air into the room and a suction unit that takes air to be cooled into the AC unit. Lastly, the kitchen duct is used when the kitchen stove operates for cooking. Air discharged from the room due to kitchen exhaust is balanced by the supply of fresh air from the door inlet and the hot air from the stove. The flow rate, temperature (where applicable) and area of each surface of the ventilation-cooling system is summarized in Table 1.

2.4.1. Cases

The level of air circulation in the restaurant depends on which of the three sub-systems, i.e. ventilation system, AC and kitchen exhaust, are in use. Selective usage of the three can result in significantly different mixing and air dispersion levels within the room.

Table 1
The flow rate and temperature setting of the ventilation system components.

	Area (m^2)	Temperature (K)	Flow rate (m^3/h)		
Ventilation			On	On	On
AC			On	On	Off
Kitchen duct			On	Off	Off
Ventilation inlet	0.09	301	540	540	540
Ventilation exhaust	0.09		−440	−440	−440
Toilet exhaust	0.7464		−100	−100	−100
Kitchen duct	0.24276		−1156	0.000	0.000
Door gap inlet	0.7898	301	1000	0.000	0.000
Stove	0.035	383	156	0.000	0.000
AC suction	0.4185		−1680	−1680	0.000
AC inlet	0.155	293	1680	1680	0.000

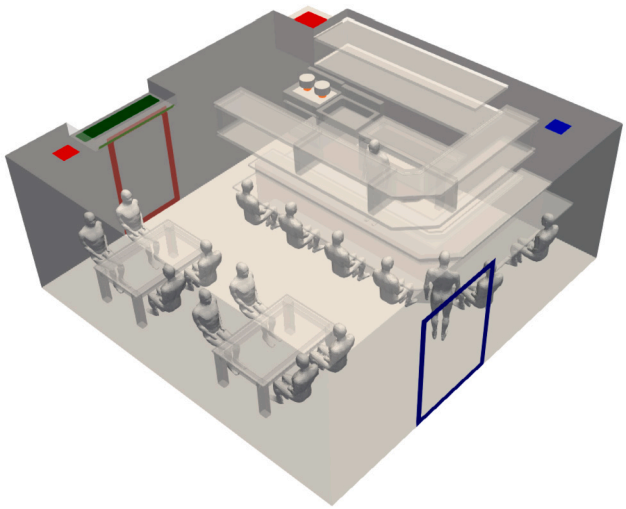

Fig. 3. The setup of the 'far seating' case corresponding case 5 in Table 2.

Table 2
Ventilation system condition of the cases being evaluated in this work.

No.	Type	Ventilation	AC	Kitchen Duct
Case 1	Close seating	ON	OFF	OFF
Case 2	Close seating	ON	OFF	ON
Case 3	Close seating	ON	ON	OFF
Case 4	Close seating	ON	ON	ON
Case 5	Far seating	ON	ON	ON

The air-exchange rate of the setup decreases from 12.8 hr^{-1} to 4.5 hr^{-1} when the kitchen exhaust is not in use. Note that AC does not contribute to air exchange. Therefore, its use or the lack of it does not add to the air-exchange rate of the room. An alternate setup shown in Fig. 3 is considered to study the effect of change in the physical distance between subjects. The geometry and the air circulatory system of the setup remain unchanged. However, the position and placement of the human subjects are modified. Firstly, the table size of both the tables within the setup is increased from 120 cm × 60 cm × 75 cm (along x, y, and z direction) to 160 cm × 108 cm × 75 cm. The change in table size increases the gap between the subjects seated across the table from 84 cm to 169 cm. The gap between subjects on the same side of the table increases from 60 cm to 68 cm. Similarly, the subjects at the kitchen counter are seated away from each other with their heads facing forward, as shown in Fig. 3.

Based on the considerations of selective usage of the ventilation-cooling system, inclusion or exclusion of the partition and distance between the subjects, we formulate five cases for the present study. The details of each case are provided in Table 2.

2.5. Simulation conditions

The numerical simulations are carried out using an in-house solver known as the CUBE [24]. The numerical mesh adopted for the mesh is shown in Fig. 4. The numerical mesh is based on the block-structured hierarchical meshing technique known as the building cube method (BCM) [25]. The cubic blocks of the mesh, known as cubes, are shown in the figure. The cubes are further subdivided

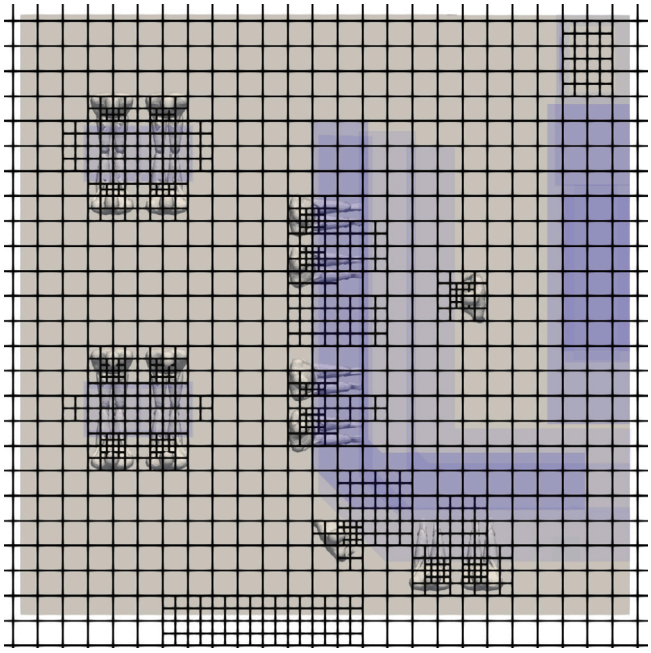

(a) Top view

(b) Side view

Fig. 4. (a) Top and (b) side view of the cubes (block discretization) of the numerical mesh. The cubes are further subdivided to contain 16 cells in each direction.

into 16 units in each direction to form the numerical cells. The mesh spacing around the mouth geometries where the speaking flow emanates is 4.27 mm. The region near the mouth, at least up to 0.5 m, has an 8.52 mm mesh allocated. All other regions within the restaurant geometry, including the wall, have a mesh spacing of 17.08 mm. The Roe scheme [26] has been employed to model the advective term in this study. This method inherently introduces a level of numerical diffusion, which effectively contributes to the required sub-grid scale diffusion that underpins large eddy simulations, as delineated in the work of Grinstein et al. [27]. The Roe scheme used for the convective fluxes in our solver allows for implicit large eddy simulations (ILES). All the geometry surfaces are modelled with an immersed boundary method to impose no-slip and isothermal/adiabatic boundary conditions [28]. The surface temperature of the human model is set to 300 K to consider the effects of buoyancy-driven flow. While the ASHRAE Handbook suggests a skin surface temperature of approximately 307 K (34C), in our model we have opted for a simplified approach using a temperature of 300 K. This decision is predicated on the assumption that in real-world scenarios, individuals are often clothed, with clothing surface temperatures typically ranging from 26C to 28C [29,30]. While the temperature of exposed body parts such as the face and hands may be higher, the adopted value simplifies the thermal boundary conditions applied to the human body surface in our model. The initial conditions for the simulation are set to standard temperature and pressure (STP) conditions, with a temperature of 297 K, a pressure of 101.3 x 103 Pa, and a relative humidity of 60%. A circular mouth geometry, placed 1 cm in front of the human model's mouth, is used to model the speaking flow, which is imposed on the circular mouth geometry. The relative humidity of the flow emanating from the mouth geometry is set to 95%. The relative humidity of ventilation inlet, door gap inlet, stove and the AC inlet is set to 60%. Neumann boundary condition is used for all the outflow vents of the room. Droplets generated from speaking are injected into the computational domain at random locations on the circular mouth geometry, with an initial velocity of 0 and temperature of 308 K, matching the temperature of the inside of the human mouth. The density of the droplets is set to 1000 kg/m^3. Before starting the speaking model, the simulations of all the cases are prerun for 100 s to develop the flow partially. After the initiation of the speaking model, the simulations are run for at least 100 seconds.

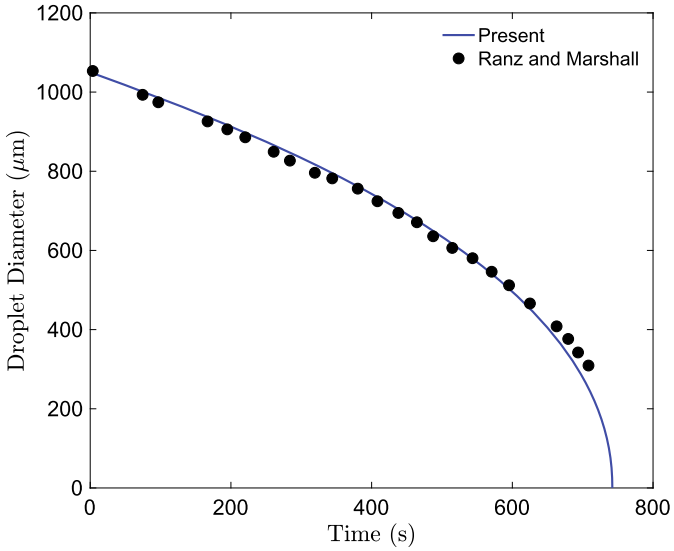

Fig. 5. The evolution of the droplet diameter as it evaporates compared with the experimental data of Ranz and Marshall [31,32].

3. Results

3.1. Validation

To verify the accuracy of our droplet model, we conduct a numerical simulation of a single droplet evaporating in an isolated environment. We use the experimental study of droplet diameter evolution by Ranz and Marshall [31,32] as a reference to validate our simulation. The simulation is set up to match the experimental conditions, in which a droplet with an initial diameter of 1050 μm is placed in a controlled environment with a relative humidity of 0% and a temperature of 298 K. The droplet's internal initial temperature is 282 K. After the droplet is exposed to the surrounding environment, we track the evolution of its diameter as it evaporates and compare it to the experimental data from Ranz and Marshall. The comparison is shown in Fig. 5, demonstrating excellent agreement between the simulation results and the experimental data.

To validate our methodology, it's important to note the extensive validation performed for the underlying flow solver used in this study, which we referenced in two significant works. The study by Li et al. [28] successfully validates our flow solver for natural convection problems, showing it can effectively handle the complexities of natural convection scenarios, including varying thermal gradients and fluid dynamics. Additionally, a comprehensive study by [33] further validates our flow solver across a wide range of applications, including no-slip, adiabatic, and isothermal boundary conditions in complex geometries. These validations support the reliability of our simulation results, even in the absence of direct validation data for our specific geometric setup.

In the context of the specific geometry we consider in this work, direct validation is difficult due to the absence of benchmark data. However, to validate our methodology, it's important to note the extensive validation performed for the underlying flow solver used in this study [28,33]. In [28], we have successfully validated our flow solver for natural convection problems, showing it can effectively handle the complexities of natural convection scenarios involving adiabatic, and isothermal boundary conditions. Additionally, in a comprehensive study [33] we have further validated our flow solver across a wide range of applications.

3.2. Droplet dispersion

A snapshot of the droplet dispersion in a restaurant is shown in Fig. 6 when only the ventilation system is turned on, and all other systems are turned off. The ventilation system consists of a fresh air inlet and a primary exhaust, which are listed in Table 1. The overall air circulation in the restaurant does not appear to be very strong. The figure shows the evolution of the droplet dispersion with time. The droplets are coloured according to the source ID and grouped into a set of four in each group. The droplets generated by the subjects on each table are coloured the same, and so on. As the simulation has been prerun for 100 s to develop the flow before the beginning of the droplet injection, the pre-existing flow due to the ventilation results in mild dispersion of the droplets due to subjects 13 and 15, seated near the fresh air inlet, even in the early stages of the simulation, as can be seen at time instants 20 and 40 s in the figure. This is in stark contrast to the behaviour of the droplets generated by the subjects (1-8) on the tables. The droplets due to subjects 1 to 8 are primarily restricted to a region around and over the table. The speaking jets emanating from subjects seated opposite each other tend to interfere, cancelling each other out. Therefore, due to the interference of the speaking jets, droplet dispersion is hindered and restricted to a region around the table. On the other hand, while the droplets due to subjects 9 to 10 and 16 may not be strongly influenced by circulation caused by the fresh air inlet, they nevertheless undergo higher dispersion when compared to those of subjects 1 to 8. As opposed to the case of subjects seated at the table, the speaking jet of the subjects at and inside the kitchen counter is unobstructed, allowing the droplets to travel further and undergo more dispersion.

Fig. 6. Snapshot of droplet dispersion at time instants 20 s, 40 s, 60 s and 80 s of Cases 1 to 5. The top row of images correspond to Case 1, the next row to Case 2, so on and the bottom row to Case 5.

The evolution of droplet dispersion for case 2, where the ventilation and kitchen duct are in operation, is presented in the second row of Fig. 6. The mass flux of air exiting the room through the kitchen duct is balanced by adding fresh air through the door gap, as indicated in Fig. 2, and the stove exhaust into the room. The operation of the kitchen duct results in far greater air circulation within the room compared to the operation of only ventilation. This is evident from the greater droplet dispersion of subjects 5 to 16, even in the early stages of the simulation. For example, at $t = 40$ s, the degree of droplet dispersion is far greater than the droplet dispersion of the only ventilation case, even at $t = 80$ s. The airflow from the door gap to the kitchen duct tends to carry the droplets of the subjects at the kitchen counter towards the kitchen exhaust, resulting in the dispersion of the droplets in question. The flow from the door gap to the kitchen duct results in a secondary flow around the table of subjects 4 to 8, aiding in the dispersion of the droplets. The droplets of subjects 1 to 4, however, are not significantly influenced by the operation of the kitchen duct. The degree of dispersion of these droplets is not significantly different from the only ventilation case.

Next, snapshots of droplet dispersion of case 3, wherein the AC, in addition to the ventilation, is in operation, are shown in row 3 of Fig. 6. The air conditioning system is located near the ventilation exhaust over the toilet exhaust, towards the top left corner of the figure. The operation of the AC directs a cold air jet towards the ground at an angle of 30 degrees to the ceiling. To balance the mass flux of air from the AC into the room a corresponding flux of air is taken out of the room through the AC suction. As the AC jet directly interferes with the subjects on the two tables, the droplets generated by subjects one to 8 undergo significant dispersion as opposed to the only ventilation case. In addition to causing significant mixing around the table area, the AC jet also results in air circulation around the kitchen counter and kitchen area dispersing the droplets generated by subjects 9 to 12 and 16. The droplet dispersion of subjects 12 to 14, which were already getting dispersed due to the fresh air of the ventilation inlet, gets enhanced by the bulk flow caused by the AC.

In the last rows of Fig. 6, the evolution of droplet dispersion for cases 4 and 5 are presented, respectively. In these cases, the ventilation, air conditioning and kitchen duct are all in operation simultaneously, resulting in the greatest amount of air circulation within the room. Consequently, the droplet dispersion in cases 4 and 5 is better than in the previous three cases. Even at very early stages, for example, at 20 seconds, the degree of droplet dispersion for cases 4 and 5 appears to be higher than in cases 1, 2 and 3. The dispersion of droplets from subjects 1 to 8 seated at the tables is more influenced by the flow due to the AC, while the kitchen duct more influences the dispersion of droplets from the subjects seated at the kitchen counter. Therefore, the dispersion pattern over the tables can be expected to be similar between cases 4 and 3, and the dispersion pattern around the kitchen counter can be expected to be similar between cases 4 and 2. However, the combined effect of the AC and kitchen duct in case 4 results in greater droplet dispersion either over the tables or around the kitchen counter compared to the independent use of the AC and kitchen duct with fresh air ventilation. Specifically, comparing cases 4 and 3, it is found that the droplet dispersion over the tables is significantly higher. In particular, the droplet dispersion around subjects 1 to 4 shows a greater difference between these two cases. A similar observation can be made when comparing the droplet concentration in the region between the kitchen counter and the kitchen duct in cases 4 and 2. Next, focusing on a comparison between cases 4 and 5, it can be seen that despite the same ventilation settings, the dispersion pattern, particularly around subjects 1 to 8, is significantly different. The greater distance between the subjects seated across the table in case 5 results in less interference between the speaking jets, which allows for greater dispersion of droplets from the subjects in question. Consequently, the effect of destructive interference between the speaking jets seen in case 4 is not observed in case 5. Contours of the time-averaged velocity magnitude on a horizontal plane for cases 1 to 5 presented in Fig. 7a-e demonstrate the variation of the flow patterns which affect the droplet dispersion discussed in this section.

3.3. Characterization of infection risk

The dose-response model used for predicting infection probability due to virion inhalation will be used in this work to characterize the droplet dispersion. The probability of infection, expressed in terms of the number of virions inhaled N assuming that N_0 virions is the minimum infection dose, is given by [37–39]

$$P = 1 - e^{\left(-\tau \frac{N(x,T)}{N_0}\right)} \tag{1}$$

where τ is the transmissibility of a given virion strain in question, the number of inhaled virions N depends on the duration of exposure T to the virions and the spatial location x of the subject inhaling them. [40]. The number of virions inhaled $N(x,T)$ can be estimated based on the number of sputum droplets a susceptible subject may inhale. For this, we track the number of droplets in a spatial region defined such that the air within this region is likely to be inhaled by a susceptible subject. This region is referred to as the inhalation zone and is illustrated in Fig. 8. For simplicity, a rectangular area around the mouth and nose was chosen to represent the inhalation zone. Fig. 8 provides examples of the inhalation zone where one of the infected subjects is modelled as the source of droplets/aerosols. In contrast, the remaining subjects are treated as susceptible to infection. For every susceptible subject, a separate inhalation zone is designated. Each subject's infection probability is evaluated by tracking the droplets in their respective inhalation zones. For this study, a 10 x 10 x 15 cm rectangular region was used to model the inhalation zone. The box size is chosen to be approximately in the same order as the inhalation volume of the speaking model adopted in this work. The inhalation zone is a rectangular box with the longer side oriented in the direction from the nose to the ground. The centre of one edge of the top face of the box is placed at the bottom edge of the nose, and an adjacent face is in contact with the outer surface of the subject's mouth. The inhalation zone is positioned so that its entire volume is outside the subject's body. The number of inhaled virions depends on the size of the sputum at the time of ejection, the density of virions in the saliva, the duration for which inhaling subject is exposed to the respiratory droplet, the volume of the inhalation zone and the breathing rate of the inhaling subject. The details of how it is arrived at can be found in literature [40,36]. Assuming that $\overline{v}_0(x)$ is the average rate of inhalation of sputum droplets expressed in terms of initial droplet volume at location x, $N(x,T)$ can be written as

$$N(x,T) = \frac{B\lambda\overline{v}_0(x)T}{V_B}$$

where B is the subject's breathing rate, λ is the viral load or viral density of the virus under consideration expressed as the number of copies per unit volume of sputum, and v_B is the volume of the inhalation zone. Note that Exposure time T is different from the simulation time. For characterizing the person-to-person infection risk, we will consider SARS-CoV-2 as the source of the airborne disease. For SARS-CoV-2, the values of the key parameters in the previous two equations are listed in Table 3.

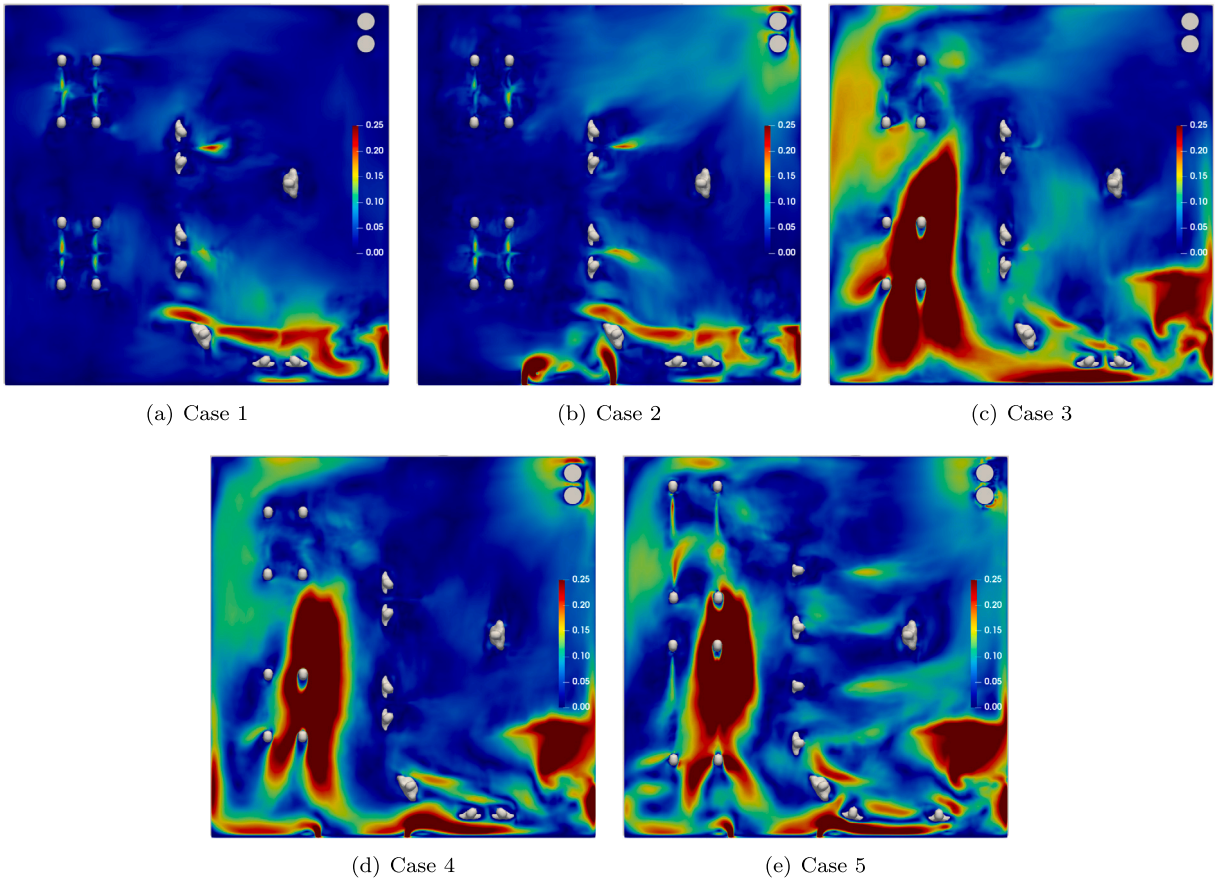

Fig. 7. Time averaged contours of velocity magnitude on a horizontal plane located at a distance of 1.2 m from the ground.

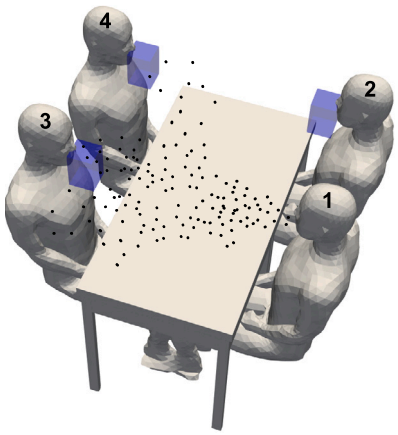

Fig. 8. An example of inhalation zone defined for susceptible subjects seated around an infected subject in order to count the respiratory droplets that enter it.

Table 3
Values of parameters in the infection risk model adopted in this work and those reported in the literature.

Parameter	Range in literature	Chosen Value
Breathing rate B (m^3/h)	0.540.21± [34]	0.5
Viral load λ ($\#copies/ml$)	Mean-7×10^6; Maximum-2×10^9 [35]	10×10^6
N_0 ($\#copies$)	300-2000 [36]	900
Inhalation zone volume V_B (m^3)	-	0.0015

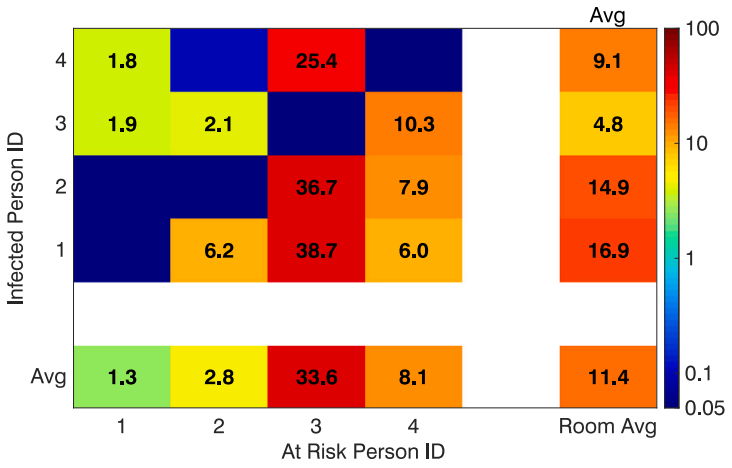

Fig. 9. A sample risk matrix with dummy entries for a hypothetical case involving four subjects.

3.3.1. Risk mapping

Taking into account the infection probability model outlined above, in the context of the restaurant simulations, we can evaluate the infection risk of each subject due to an infected subject. A scenario with only one infected subject and multiple subjects at risk simplifies this analysis, yet this cannot be broadly applicable to every situation, thus limiting its utility. For instance, if we assume that subject 1 is infected, the simulation results will only be valid if the infected person is seated at subject 1's location. However, if the infected individual is at another location, the simulation results may not be reliable or applicable. Therefore, it's essential to consider 16 mutually exclusive scenarios in which one of the 16 subjects is infected, and analyze the infection risk of the remaining 15 subjects. In evaluating the infection risk the following assumptions are made vis-a-vis the restaurant setup.

- N mutually exclusive scenarios are considered with one of the N subjects acting as the source of infection in each scenario.
- There is only one source of infection in each scenario. Multiple sources of infection in a given scenario are not considered.
- The behavioural patterns, such as speaking duration, loudness, infectiousness, of the infection source in each scenario is the same.
- The remaining N-1 subjects are at risk due to the single infection source in each scenario.
- All the seats of the restaurant are fully occupied in each scenario.

Such an analysis would result in one set of infection probability for each uninfected subject for a given scenario. For N scenarios, n sets of results would be generated, thereby expanding the dataset considerably. To analyze the resulting dataset of each simulation, a risk map or risk matrix presents an intuitive and visual method.

To illustrate the construction and interpretation of a risk matrix, let's consider a sample setup involving four subjects, as shown in Fig. 8. We assume that all four subjects generate respiratory droplets during the simulation, with each subject's droplets assigned a unique ID. This unique ID enables us to trace the droplets from a particular source entering the inhalation zone of a susceptible subject independently. For instance, considering subject 2, we track and count the droplets from subjects 1, 3, and 4 separately, subsequently evaluating their respective infection risks. The infection risk of each of the four subjects resulting from the other three subjects is then represented as a risk matrix, as displayed in Fig. 9. Note that the risk values presented here are arbitrary and are chosen solely for illustrative purposes.

The matrix is organized into a 6×6 grid, with the primary 4×4 submatrix at the top-left corner representing the person-to-person infection risk. Rows and columns labeled as "5" are placeholders, providing a visual separation between the primary submatrix and the final row and column. The rows of the 4×4 submatrix are labeled as "Infected Person ID," while the columns are labeled as "At Risk Person ID." Each row shows the infection risk of the remaining three subjects due to the subject corresponding to that row ID. For instance, the first row corresponds to Subject 1, and each entry displays the infection risk for Subjects 2, 3, and 4. By definition, the first entry in this row will be zero, as a subject cannot infect themselves.

The bottom row labeled "Avg" represents the average infection risk each subject faces due to the other subjects. For instance, the average infection risk of Subject 1 due to Subjects 2 to 4 is 1.3%. What this implies is that 3 different scenarios in which subjects 2, 3 and 4 are infected were considered to evaluate the average risk to subject 1 from the remaining 3 subjects. Similarly, the rightmost column labeled "Avg" represents the average infection risk posed by a given subject to all other subjects. For example, the average infection risk posed by Subject 4 is 9.1%. Lastly, the matrix's bottom-right entry labeled "Room Avg" represents the average infection risk across the entire system, assuming any subject could randomly become infected. By definition, the "Room Avg" value equals the mean of the "Avg" column or the "Avg" row. The Room Avg infection risk's evaluation in equation form is presented in Section 3.4.

Next, the results of the present study in the form of a risk matrix will be presented and discussed. The ID of the subjects in the restaurant setup is shown in Fig. 10. In Fig. 11a, the risk matrix of Case 1, in which only fresh air ventilation is in operation, is presented. The person-to-person infection risk of all 16 subjects in the restaurant environment is shown in the risk matrix. As

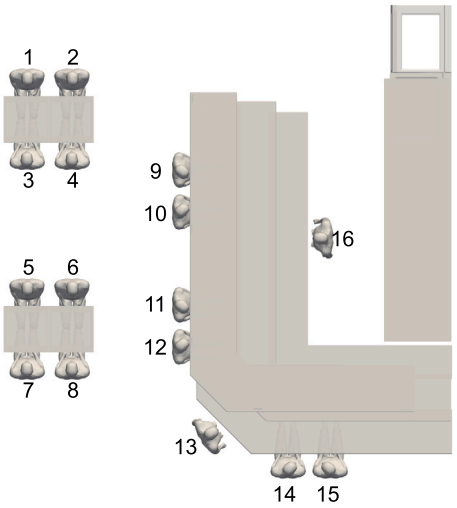

Fig. 10. The numbering of the subjects in the restaurant that will be used for the risk mapping.

discussed in Section 3.2, the droplet dispersion, in this case, is minimal, resulting in droplets from each table being restricted to their respective tables, with minor dispersion at the kitchen counter. Consequently, the infection risk of subjects 1 to 4 is restricted to subjects 1 to 4, and the same is true for subjects 5 to 8. Due to the ventilation exhaust over subject 1 on the roof, there is an asymmetry in the probability of infection between subjects 1 to 4. It is seen that the risk of infection for subjects 2 to 4 is significantly lower than the infection risk for subject 1. The infection risk for subject 1 due to subjects 2 to 4 is consistently high, while this is not the case for subjects 3 and 4; subject 2 is marginally worse off compared to subjects 3 and 4. This asymmetry is due to the tendency of the droplets to move towards the ventilation exhaust, which is located over subject 1, resulting in subject 1 coming in contact with the droplets of subjects 2 to 4 while the reverse is not true. None of the subjects other than subjects 1 to 4 is at risk due to subjects 1 to 4.

In the case of subjects 5 to 8, an asymmetry in the infection risk is also observed, with subject 6 at a higher risk compared to the other three subjects and subject 7 displaying an extremely low infection risk. Unlike the situation with subjects 1 to 4, where they do not pose a risk to the remaining subjects, some droplets from subjects 6 and 8 move towards the kitchen counter, resulting in subjects 11 and 12 being at negligible risk. As the most dispersion in Case 1 occurs near the kitchen counter, there is more scattering in the entries corresponding to subjects 10 through 16 in the risk matrix. Furthermore, as the flow has to traverse from the ventilation inlet, located at the bottom right corner, when viewed from top, to the ventilation exhaust located at the top left corner, the droplets from the kitchen counter tend to move towards the tables. As a result, subjects 6 and 8 come into contact with droplets from many of the subjects near the kitchen counter, resulting in a non-zero infection risk. This can be noted from the columns corresponding to subjects 6 and 8 in the risk matrix. It is also interesting to note that, as subject 16 is isolated from all the remaining subjects, the risk to subject 16 is minimal and subject 16 seems to come into contact with only the droplets of the subject directly in front of subject 16. The row at the bottom of the matrix shows the average infection risk each subject is exposed to due to contaminants from the other remaining subjects. Similarly, the column on the right of the infection matrix presents the average infection risk all the subjects face due to the contaminants of any given subject. The lower left entry of the matrix shows the room's average infection risk, which is about 5.5%. This may be interpreted as the infection risk of the entire room, assuming any one subject at random may be infected.

The risk matrix of case 2, in which the fresh air ventilation and kitchen duct are operating, is shown in Fig. 11b. A significant difference immediately apparent when comparing cases 1 and 2 is that the amount of scatter has increased in the risk matrix of case 2. While the situation for subjects 1 to 4 has not changed significantly, the infection risk of subjects at the other table has increased due to the dispersion and mixing of droplets from the remaining subjects, particularly those at the kitchen counter. Another major difference that can be noticed immediately is that the infection risk for subject 16 has significantly increased due to the operation of the kitchen duct, which carries droplets from the subjects at the kitchen counter towards subject 16. It is also interesting to note that while, on average, the dispersion of droplets results in a lower infection risk for everyone, some subjects experience a higher infection risk, such as subjects 4 and 5, which can be seen in the bottom row of the matrix.

In addition to the fresh air ventilation in case 3, the air conditioning system's operation results in even more scattering of the entries in the risk matrix shown in Fig. 11c. The cool air jet from the AC interacts with the droplets generated by the subjects seated at the table, dispersing and transporting the droplets throughout the room. As a result, the distribution of risk in the risk matrix for subjects 1 to 8 is markedly different from that of cases 1 and 2. The contaminants from subjects 1 to 4, in addition to affecting each other, managed to reach subjects 5 to 8 seated on the other table and some of the subjects seated at the kitchen counter. Similarly, subjects 1 to 4 are not only at risk from each other but also at risk from subjects seated at the other table and the kitchen counter, as well as the kitchen staff. The reason for the contaminants from the kitchen counter reaching subjects 1 to 4 is the air conditioning suction and the ventilation exhaust. While more non-zero entries in the risk matrix indicate a higher probability of person-to-person infection, the average infection risk for each person can still be lower. Focusing on the bottom row of the risk matrix, it is seen that,

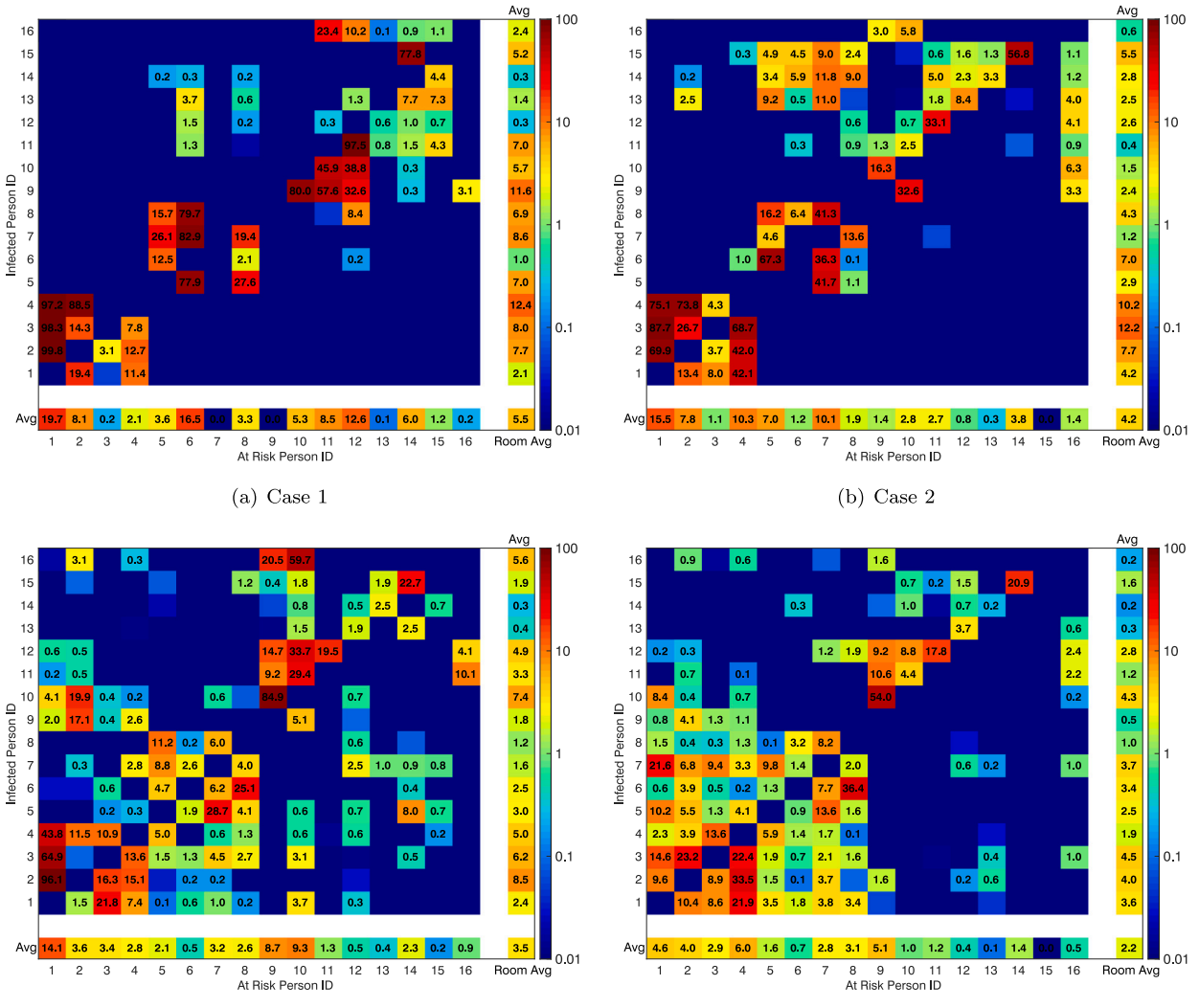

(a) Case 1

(b) Case 2

(c) Case 3

(d) Case 4

Fig. 11. Risk matrix plotting the probability of infection for an exposure duration of $T = 60$ mins for Cases 1 to 4.

on average, most subjects experience a lower infection risk than cases 1 and 2. However, the infection risk for some subjects, like subjects 9 and 10, is higher for this case compared to cases 1 and 2.

The amount of scatter in the risk matrix of case 4, in which the AC, fresh air ventilation, and kitchen duct are operating, is not significantly different from case 3. The risk matrix of case 4 is presented in Fig. 11d. While the level of scatter may not be different from case 3, the scatter pattern seems different. The operation of the kitchen duct, in addition to the AC, significantly alters the flow around the kitchen area. The operation of the kitchen duct also includes fresh air coming into the room from the main door. The interaction of the AC jet with the air coming in from the main door results in a flow pattern that restricts the droplets generated by subjects 1 to 8 around the table region and, to some degree, restricts their transport to the kitchen area (see Fig. 1). As a result, the contaminants of subjects 1 to 8 do not affect the subjects around the kitchen counter as much as they do in case 3. This is evidenced by the mostly zero entries in the bottom right region of the risk matrix in Fig. 11d. The converse of this, the contaminants of subjects from the kitchen area affecting the subjects on the tables, appears to be similar between cases 3 and 4. Interestingly, the subjects closest to the AC appear to be strongly influenced by the operation of the kitchen duct. Compared to case 3, the infection risk of subject 1 appears to have reduced significantly, while that of subjects 2 and 4 appears to have increased marginally. It is also worth noting that the average infection risk of subjects 9 and 10 seems to have reduced significantly.

Finally, the risk matrix of case 5 is presented in Fig. 12. The ventilation setting of case 5 is identical to case 4, but the seating arrangement of the subjects is different, as shown in Fig. 3. The level of scatter in the risk matrix is similar to cases 3 and 4, with a slight difference in the scatter pattern compared to case 4. The average infection risk of each subject is lower than any of the previous cases, as can be seen from the bottom row of the risk matrix, with a couple of exceptions, like subject 3.

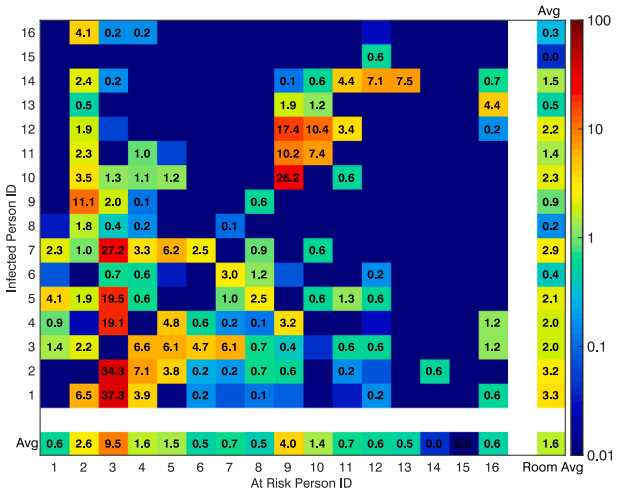

Fig. 12. Risk matrix for Case 5 for an exposure duration of $T = 60$ mins.

3.4. Room average risk

We use individual infection risk data to calculate both person and room average infection risks subject to the assumptions listed in Section 3.3.1. To understand the average risk of infection for a subject j considering the N mutually exclusive scenarios, we introduce the following relation,

$$P_{\to j}^{avg} = \frac{1}{N-1} \sum_{i=1}^{N} P_{i \to j}$$

In this equation, $P_{i \to j}$ symbolizes the probability of subject j getting infected due to subject i in scenario i, and N represents the total number of mutually exclusive scenarios in which one of the subjects is infected. Note that we have adopted a convention where subject numbered i is the infection source in scenario i. The term $P_{\to j}^{avg}$ represents the average infection risk of subject j due to the infected subject of each of the N mutually exclusive scenarios. This equation doesn't imply that all subjects can infect subject j simultaneously. Instead, it aids in estimating a comprehensive risk profile for subject j by considering the possibility of one subject in each scenario i being a source of infection.

The next equation represents the average infection of scenario i (one of the N mutually exclusive scenarios) in which subject i is the source of infection.

$$P_{i \to}^{avg} = \frac{1}{N-1} \sum_{j=1}^{N} P_{i \to j}.$$

The physical interpretation of this equation is that it provides the probability of infection for a random uninfected subject who may be seated at any one of the remaining $N-1$ positions in scenario i.

The average infection risk of the entire room, that is the infection risk for an uninfected subject who may be located at a random location in the N locations, considering the N mutually exclusive scenarios, can be described in terms of $P_{\to j}^{avg}$ or $P_{i \to}^{avg}$ as

$$P^{room} = \frac{1}{N} \sum_{j=1}^{N} P_{\to j}^{avg} = \frac{1}{N} \sum_{i=1}^{N} P_{i \to}^{avg}.$$

This equation provides a statistical measure of the overall infection risk within a room, taking into account the possibility of each subject being a source of infection individually across the N scenarios.

In the field of probability and statistics, the concept of "expected value" plays a pivotal role. The expected value is the theoretical average of a process if it were repeated many times [41]. The expected value is a key concept in a variety of contexts, such as statistics, economics, insurance, and in our case, modeling the spread of infection.

In the context of infection modeling, the expected value can be interpreted as the expected number of new infections or the number of people likely to be infected if the experiment is repeated many times by changing the infected person. The expected value allows us to quantify risk and make predictions about the future state of the system based on current observations. It forms the basis for our subsequent calculations on the infection risk within a room. In the following section, we will be using the concept of expected value to calculate the expected number of individuals likely to be infected due to a given scenario i. This will provide an overall estimation of the infection spread. The expected value due to a scenario i can be represented as:

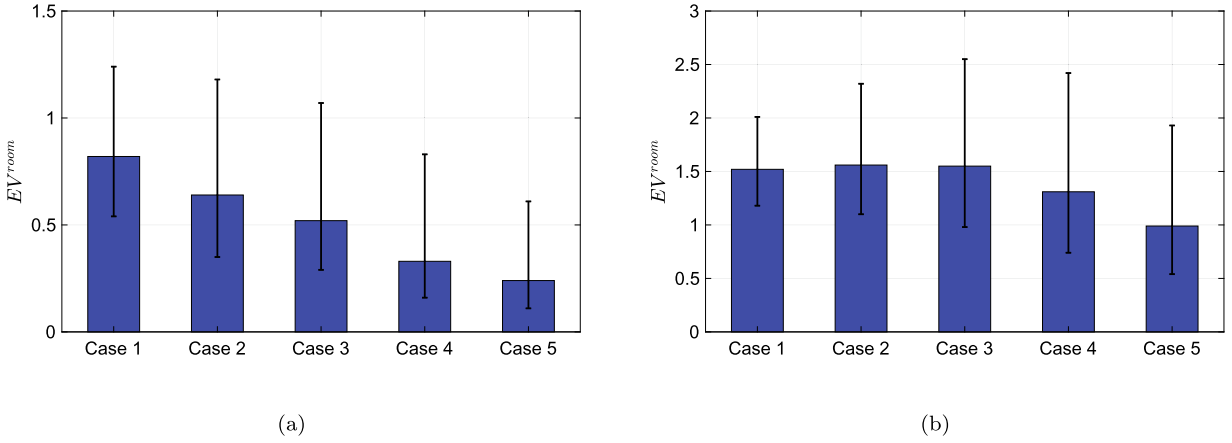

Fig. 13. Comparison of the expected value across Cases 1 to 5 for an exposure duration $T = 60$ min (a) $\tau = 1$ (b) $\tau = 5.77$. The error bars are included to indicate the changes in the expected value when N_0 is changed. The positive and the negative error correspond to N_0 of 300 and 2000, respectively.

$$EV_i = \sum_{j=1}^{N} P_{i \to j}$$

Here, EV_i represents the estimated number of infections due to scenario i. The room's expected value, or the average expected number of infections in the room considering the N possible mutually exclusive scenarios, can be represented as:

$$EV^{room} = \frac{1}{N} \sum_{i=1}^{N} EV_i.$$

Thus, the expected value for the entire room, EV^{room}, provides an estimation of the likely number of individuals to be infected considering all possible scenarios in which each subject as a potential source of infection one at a time. This representation can provide meaningful insights into the potential spread of infection within a given environment.

It is important to note that these models do not assume all subjects are simultaneously infected. Instead, they consider a range of scenarios where each subject could potentially become a source of infection individually. These models provide a statistical risk profile by averaging over these situations, representing a comprehensive measure of potential infection spread in a given room.

Also, comparing EV^{room} and P^{room}, we find a simple relationship that the room expected value, EV^{room}, equals the room average risk, P^{room}, multiplied by $(N - 1)$. This relationship forms a key aspect of our analysis, linking the average risk of infection in the room with the expected number of people likely to get infected.

The expected values for the 5 cases are presented in Fig. 13 assuming two values for the transmissibility τ. In Fig. 13a, where $\tau = 1$, the expected value progressively decreases from Case 1 to Case 5. The progressive operation of more ventilation system components lowers the room's average infection risk and the number of newly infected persons. Using either the kitchen duct or the AC lowers the room's average infection risk compared to only fresh air ventilation; however, the AC is slightly more effective than the kitchen duct. When both the kitchen duct and the AC are used along with the fresh air ventilation, the room's average infection risk is lower than the case where only one of them is in operation. In addition to using a ventilation system that includes mechanical mixing, increasing the physical distance between the subjects also appears to contribute to reducing infection risk. The error bars in Fig. 13 are presented to demonstrate how the expected values change when N_0 is altered. For $\tau = 1$, a change in N_0 does not alter the qualitative behaviour of EV^{room} across the cases.

When a higher transmissibility is assumed, $\tau = 5.77$ in Fig. 13b, the qualitative behaviour of EV^{room} is significantly altered. The role of τ in Eq. (1) is to alter the effective value of N_0. $\tau > 1$ implies that the effective N_0 is lower than the initially assumed N_0. For example, for the base variant/strain of a virion, if 900 virions are needed on average to cause infection then for a new variant/strain of the virion with higher transmissibility $\tau = 5.77$ only 156 virions are needed on average to result in infection. EV^{room} decreases from Case 1 to 5 progressively when $\tau = 1$, however, a marginal increase from Case 1 to 3 and then a decrease from Case 3 to 5 is seen for $\tau = 5.77$ for $N_0 = 900$. This tendency is accentuated for $N_0 = 300$. On the other hand, when $N_0 = 2000$, the original trend, observed in Fig. 13a, is maintained. As explained above, effect of τ is to lower N_0 by a factor of 5.77. The reason for such a change in the qualitative behaviour can be understood through a comparison of the risk matrix of cases 1 and 3 for the two values of τ considered here presented in Fig. 14a-b for case 1 and in Fig. 14c-d for case 3. The primary reason for the qualitative change in the expected value, vis-a-vis room average infection risk, is the degree of dispersion and therefore the scatter in the risk matrix of Cases 1 and 3. The infection risk in case one is localized To certain sections of the setup as discussed in the previous section, and within those sections, due to high droplet concentration, the individual infection risk is high, which contributes to a higher room average infection risk. In this case, the infection risk of many subjects is already close to saturation; increased transmissibility increases the infection risk of only those whose infection risk is low. In case 3, due to the greater dispersion of droplets individual infection risk of many

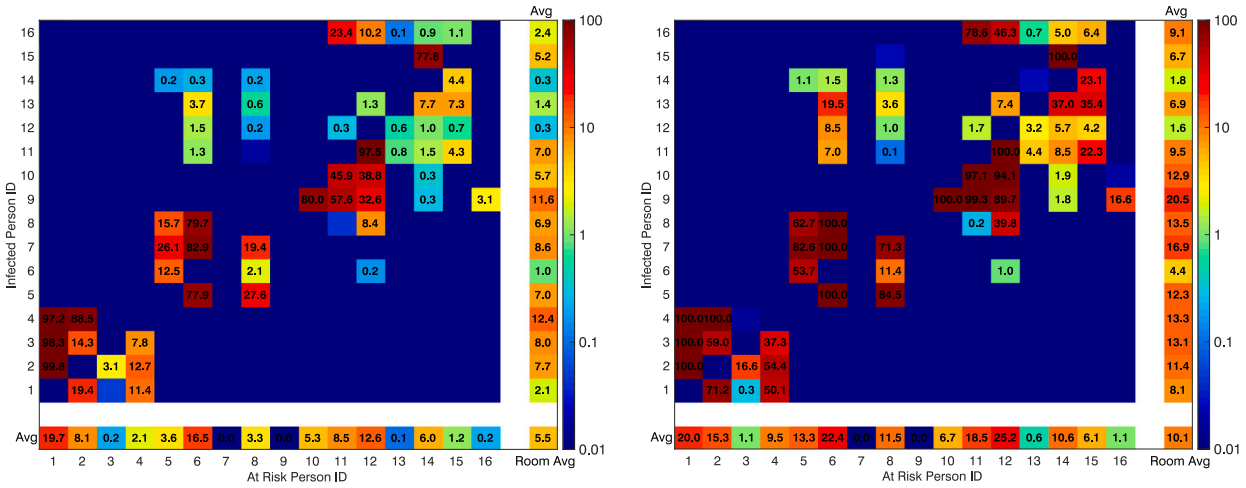

(a) Case 1: $\tau = 1$ (b) Case 1: $\tau = 5.77$

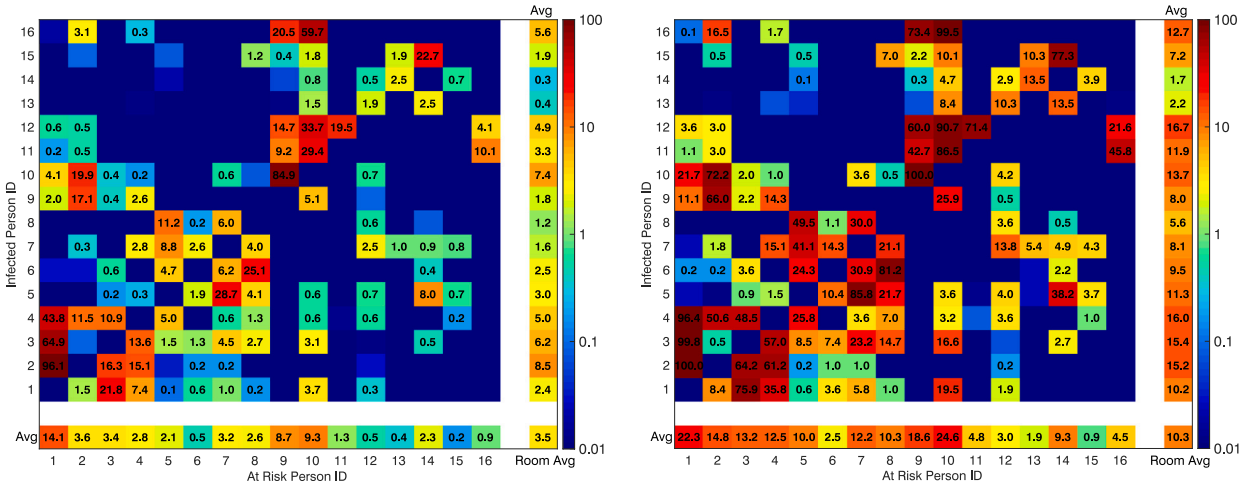

(c) Case 3: $\tau = 1$ (d) Case 3: $\tau = 5.77$

Fig. 14. Risk matrix plotting the probability of infection for an exposure duration of $T = 60$ mins for Cases 1 to 4.

subjects is relatively low. Therefore, most of the subjects experience an increase in infection risk due to increased transmissibility of the virion. Consequently, the factor by which the room average infection disk of case 3 can increase is more significant than that of case 1.

4. Discussion

In the face of global threats posed by airborne diseases such as COVID-19, SARS, and H1N1 influenza, understanding and quantifying infection risk in diverse environments is of paramount importance. This study introduces a methodology for assessing this risk, especially in indoor settings like restaurants, where multiple sources of infection are plausible, and the use of masks may not always be practical. The proposed approach leverages a statistical model derived from a droplet dispersion model and incorporates real-world variables such as droplet concentration, ventilation conditions, and exposure duration. According to the model developed in this study, infection probabilities in some scenarios surpass 90%, with a few even reaching 100%. These figures should not be viewed as definitive certainties of infection but rather as indicative of conditions highly conducive to disease transmission. They serve as a potent reminder of the need for rigorous preventive measures in such settings. Additionally, the statistical modeling and interpretation of the risk map or risk matrix are subject to the assumptions outlined in Section 3.3.1. The scenarios considered in this work, based on these assumptions, are likely to deviate from real-world conditions. For instance, a restaurant may not always have full occupancy; there may be more than one source of infection at any given time, etc. Both the analysis of average person-to-person and scenario-based infection probabilities are valid within the scope of these assumptions and will require further scrutiny in future work to accommodate more realistic conditions.

In developing the speaking model for human subjects, we assumed that all subjects are speaking simultaneously throughout the simulations. This assumption has two limitations. First, in real conversations, people speak in turns rather than simultaneously. This means that our model may overestimate the number of respiratory droplets emitted by a given subject during a specified duration. Second, when subjects are facing each other and speaking simultaneously—such as subjects 1 to 8 seated at the table in Fig. 10—the speaking flow jets create destructive interference. This reduces the distance over which droplets may be dispersed and, consequently, lowers the droplet concentration reaching a subject seated opposite the speaker. These limitations offer avenues for future work that could involve modeling speech patterns that more closely mimic real-world conversations.

The validation process examined various components of the methodology employed in this work, as detailed in Section 3.1. While this approach does not directly validate the infection risk predictions due to the inherent uncertainties involved, it does support the model's consistency and reliability. The findings of this study underscore the critical need to understand the multitude of variables contributing to airborne disease transmission. It is crucial to note that the model simplifies complex real-world dynamics and primarily serves as a tool for identifying high-risk situations rather than predicting absolute likelihoods of infection. Additional factors, such as individual immune responses, variations in the viral load of droplets, and the survival rate of the virus in the environment, could further influence transmission rates. These factors present potential avenues for the further refinement and development of the model.

5. Summary

In this work we carried out an investigation of transmission of respiratory infections in a restaurant setting. Through numerical simulations, we modeled the transport of droplets in a restaurant environment with various ventilation scenarios. In Case 1, with only the ventilation system turned on, we found that the overall air circulation was limited and droplets generated by subjects seated at tables remained mostly confined to their immediate area. However, subjects seated at the kitchen counter saw greater dispersion due to their unobstructed speaking jet. In Case 2, with both the ventilation and kitchen duct systems turned on, air circulation was improved and greater droplet dispersion was observed for both table and kitchen counter seated subjects. The addition of the air conditioning system in Case 4 resulted in the highest droplet dispersion. Increased droplet dispersion increases the possibility of a subject coming in contact with contaminants of non-proximal subjects. On the other hand, higher droplets dispersion also lowers the local droplet concentration.

To characterize the infection risk of a multi-contaminant source scenario, we developed a person-to-person risk-mapping methodology in the form a risk matrix. The Wells-Riley infection risk model was used to evaluate the infection risk of a subject due to contaminants of all other subjects to generate the risk-matrix. The key point of the methodology the ease of visually characterizing person-to-person infection risk while at the same time providing more generalizable person-average and room-average risk information. Using this method for risk-mapping several key observations were made for the 5 cases considered in this work. Firstly, a comparison of the risk-matrices across all the cases showed that the person-to-person infection risk increases with increasing mechanical mixing of air within the restaurant. The infection risk is highly localized when only fresh air ventilation is in operation in Case 1, however, due to higher droplet concentration the person average and room-average infection risk are also relatively high compared to other cases. Increased progressive mixing in cases 2 to 4 delocalizes the person-to-person infection risk. This increases the possibility of infection of a given subject if there are more than one source of infection.

We also evaluated the effect of various ventilation system conditions on the expected number of newly infected persons (or expected value), which can be treated as a proxy for the room-averaged infection risk. This approach provides information of newly infected subjects under the assumption that any one subject in the restaurant random may be infected. The expected value was evaluated assuming two values of transmissibility in the infection risk model. The results showed that using a ventilation system with mechanical mixing (fresh air ventilation, kitchen duct, and AC) decreased the expected value compared to only fresh air ventilation. The operation of the AC was found to be slightly more effective than the kitchen duct. However, increased transmissibility ($\tau > 1$) can reverse this trend and increase the expected value, even if mechanical mixing is used. The reason for this was elucidated by comparing the risk-matrices of Case 3 for the two transmissibility values. In conclusion, our study showed that ventilation and air circulation systems play a significant role in droplet dispersion and infection risk in a restaurant setting. Higher dispersion of droplets subject to mechanical may not always lead to lowering the average infection risk of an indoor setting like a restaurant. The average infection risk is strongly influenced by transmissibility of a pathogen. Low transmissibility (or high N_0 in the Wells-Riley model) of pathogen results in lower infection risk when mechanical mixing is used. On the other hand, inclusion of mechanical mixing may be inconsequential on the infection risk when the transmissibility (or low N_0) of a pathogen is high.

CRediT authorship contribution statement

Rahul Bale: Conceived and designed the experiments; Performed the experiments; Analyzed and interpreted the data; Contributed reagents, materials, analysis tools or data; Wrote the paper.

ChungGang Li: Contributed reagents, materials, analysis tools or data; Wrote the paper.

Hajime Fukudome: Contributed reagents, materials, analysis tools or data; Wrote the paper.

Saori Yumino: Conceived and designed the experiments; Contributed reagents, materials, analysis tools or data; Wrote the paper.

Akiyoshi Iida: Conceived and designed the experiments; Analyzed and interpreted the data; Contributed reagents, materials, analysis tools or data; Wrote the paper.

Makoto Tsubokura: Conceived and designed the experiments; Analyzed and interpreted the data; Contributed reagents, materials, analysis tools or data; Wrote the paper.

Declaration of competing interest

The authors declare that they have no known competing financial interests or personal relationships that could have appeared to influence the work reported in this paper.

Data availability

Simulation data can be made available upon request. Binary executable of the serial version of the CFD solver can be made available upon request.

Acknowledgements

This work was supported by JST JST-CREST, Grant Number JPMJCR20H7, Japan. This work used computational resources of the Supercomputer “Fugaku” provided by the RIKEN Center for Computational Science through the HPCI System Research Projects (Project ID: hp210086, hp220180, hp220183). R.B. acknowledges the support for this work by JSPS JSPS-KAKENHI Grant Number 22K10596.

Appendix A. Additional flow visualizations of Case 1

The vertical component of the velocity field is expected to be dominant in Case 1 due to the absence of operation of the kitchen duct and the AC. The velocity magnitude at different horizontal planes is presented in Fig. A.1, and the velocity vector plots at different horizontal planes are presented in Fig. A.2.

Appendix B. Grid convergence

In order to ensure that the results of the numerical simulation are independent of the grid size, a grid convergence study is performed. Four distinct meshes, characterized by different mesh sizes, were utilized for this investigation. The mesh spacing it the vicinity of the mouth for the 4 meshes is listed in Table B.1. The main mesh used for the present work is Grid3.

The results of the grid convergence study are visualized in Figs. B.3 and B.4. Each of these figures depicts the contours of velocity magnitude on horizontal planes for the four different grid sizes used in the study. Fig. B.3 represents the plane at Z = 1.12 m, while Fig. B.4 represents the plane at Z = 1.5 m.

Each subfigure in Figs. B.3 and B.4 corresponds to a specific grid size (Grid1 to Grid4). Upon comparison, it is observable that there is a reasonable agreement in the flow characteristics between the Grid3 (mesh size of 4 mm) and Grid4 (mesh size of 2.7 mm) simulations, suggesting that the mesh refinement between these two sizes does not significantly alter the results.

In addition to the qualitative comparison in Figs. B.3 & B.4, a quantitative comparison of the velocity magnitude at selected lines shown in Fig. B.5a is presented in Fig. B.5b-c.

Considering the agreement in the results and the computational efficiency, Grid3 is selected as the most suitable mesh for the present study. The choice of Grid3 strikes a balance between computational expense and accuracy of results, thereby ensuring a robust numerical model for further simulations. Subsequent sections will present the results and findings based on the simulations performed with the selected Grid3 mesh.

Table B.1
Grid sizes for the grid convergence study.

Case	At mouth	In front of mouth	Other regions
Grid1	17.08	34.16	68.32
Grid2	8.54	17.08	34.16
Grid3	4.27	8.54	17.08
Grid4	2.74	5.48	10.96

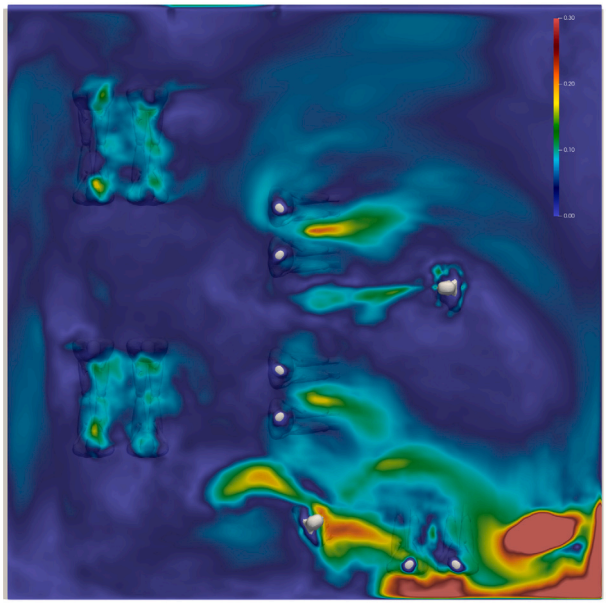

(a) $Z = 1.5\mathrm{m}$

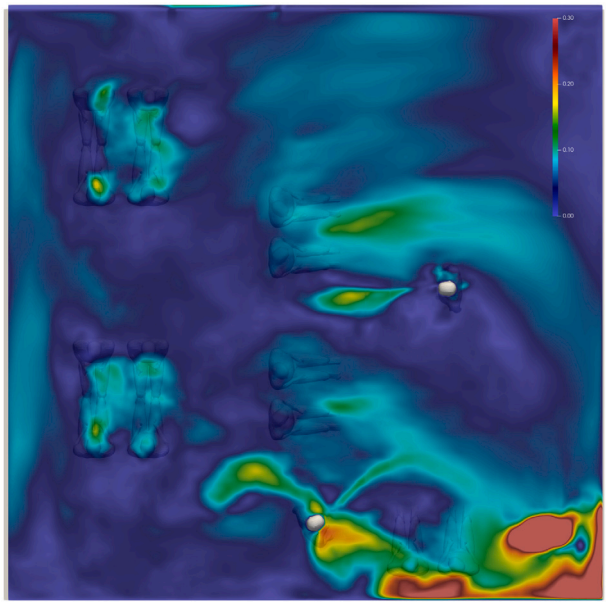

(b) $Z = 1.65\mathrm{m}$

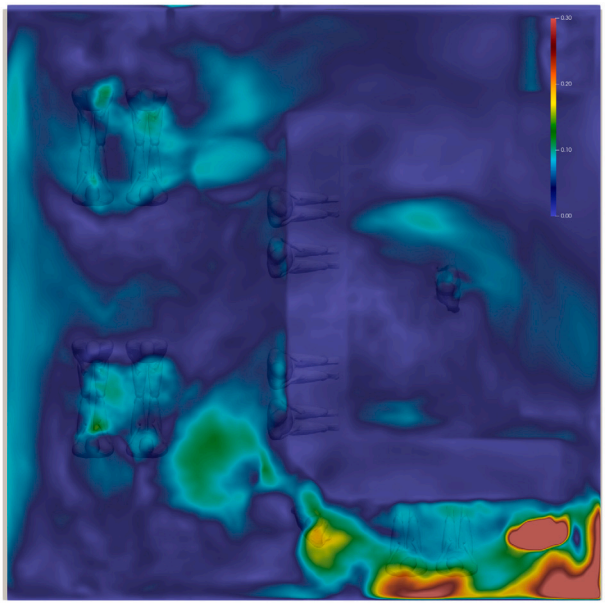

(c) $Z = 1.9\mathrm{m}$

Fig. A.1. The velocity magnitude contours of Case 1 on horizontal planes over the subjects (a) 1 to 8, (b) 9 to 12, and (c) 13 and 16. The range of the colorbar is between 0 and 0.3 on a linear scale.

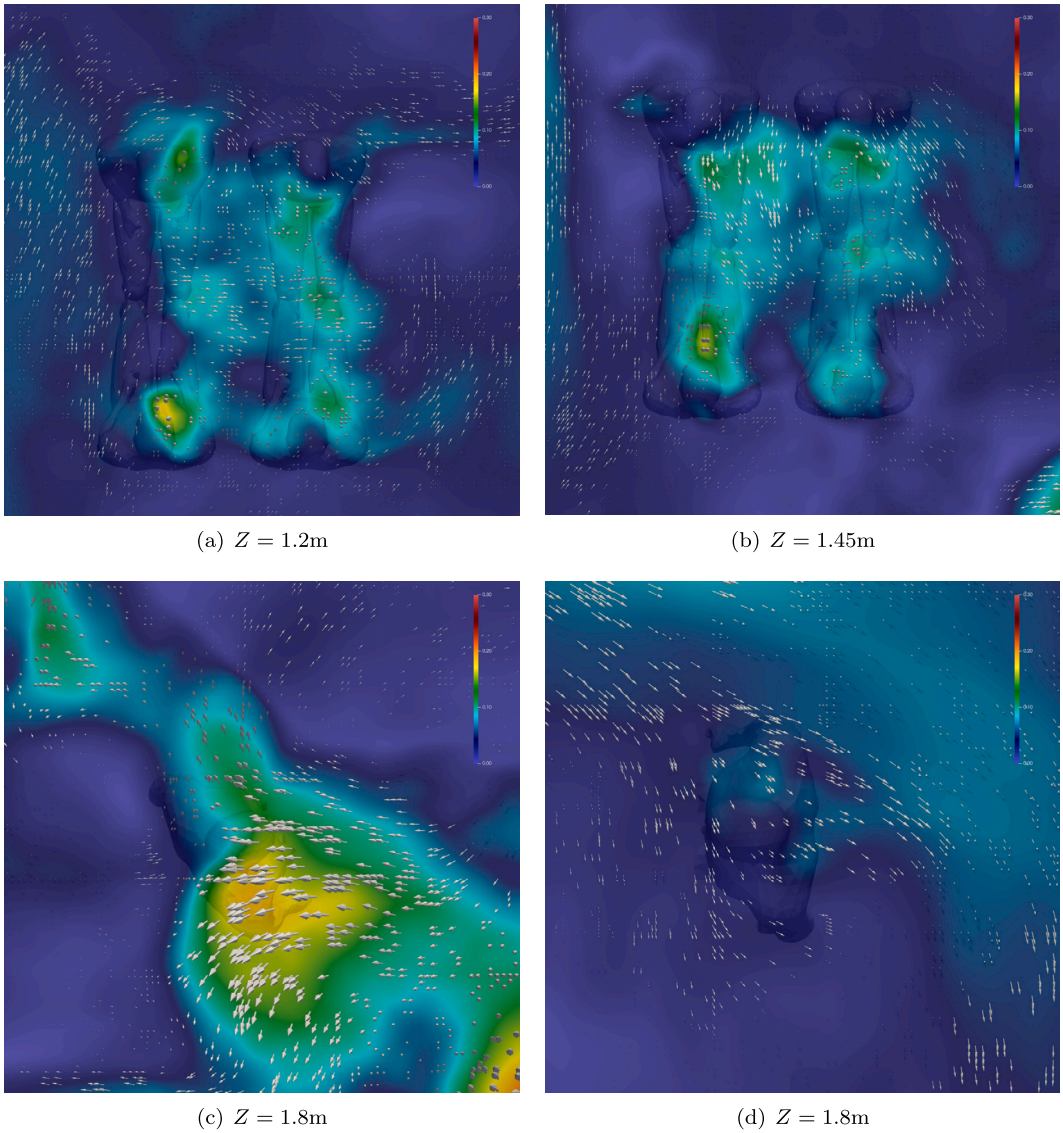

(a) $Z = 1.2\text{m}$ (b) $Z = 1.45\text{m}$

(c) $Z = 1.8\text{m}$ (d) $Z = 1.8\text{m}$

Fig. A.2. The velocity vectors and velocity magnitude plotted on horizontal planes over subjects (a)1 to 4, (b) 5 to 8, (c) 12 and (d) 16. The range of the colorbar is same as the previous figure.

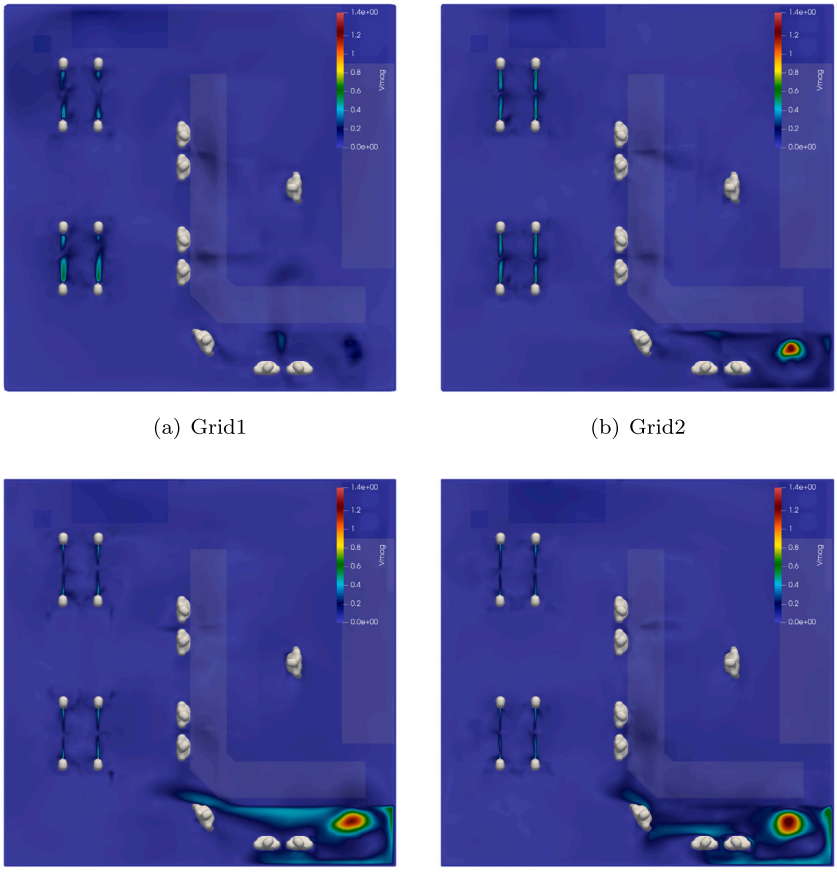

(a) Grid1 (b) Grid2

(c) Grid3 (d) Grid4

Fig. B.3. The contours velocity magnitude on a horizontal plane (Z = 1.12 m) for the 4 grid cases.

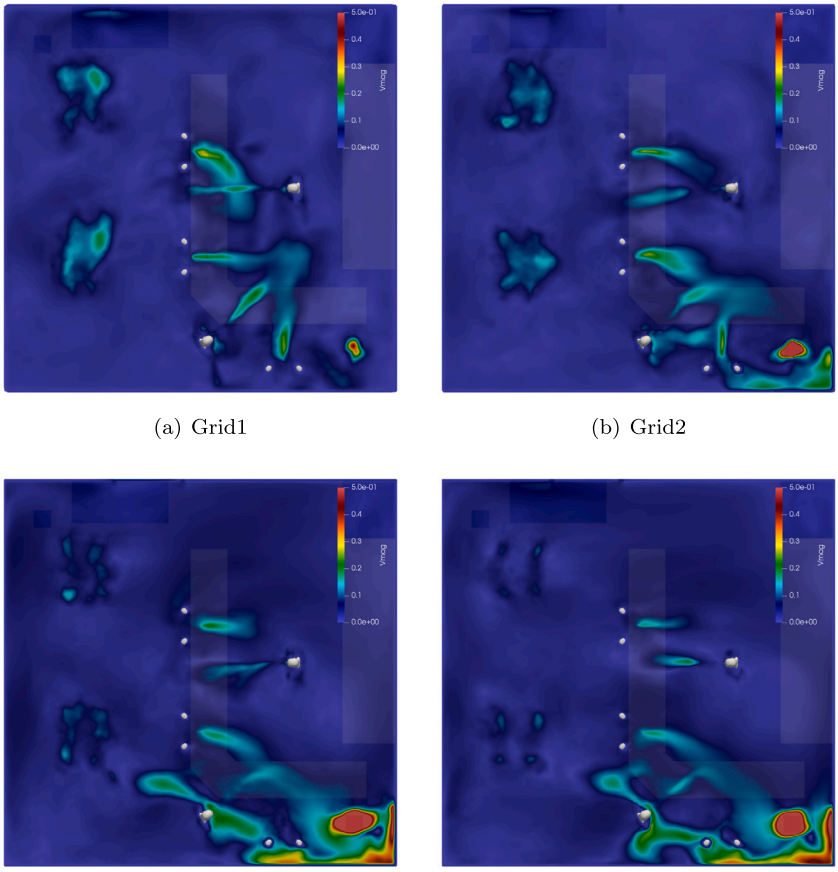

(a) Grid1 (b) Grid2

(c) Grid3 (d) Grid4

Fig. B.4. The contours velocity magnitude on a horizontal plane (Z = 1.5 m) for the 4 grid cases.

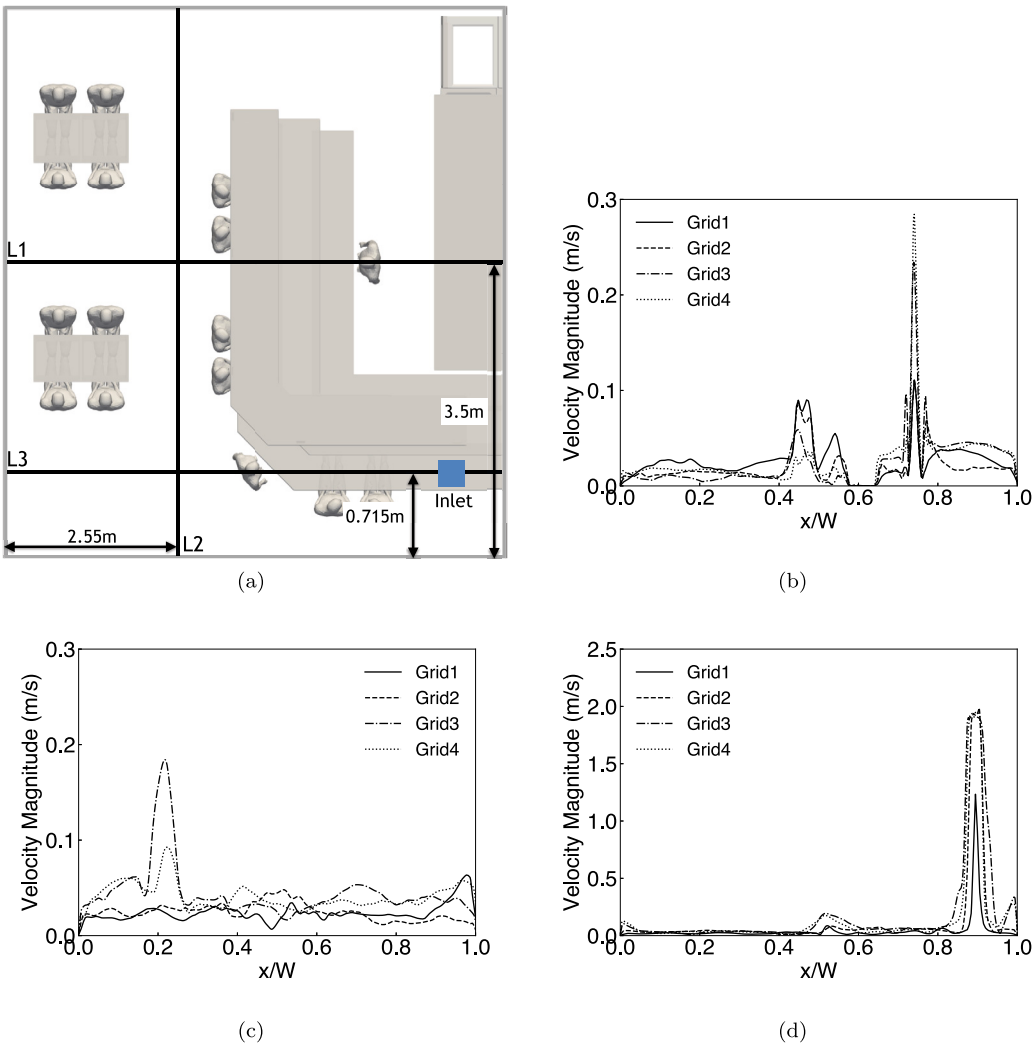

Fig. B.5. (a) Location of measurement lines: L1 ($z = 1$ m), L2($z = 1.5$ m), L3($z = 2$ m). Comparison of velocity magnitude of the four grid cases at lines (b) L1, (c) L2, and (d) L3.

References

[1] J. Wei, Y. Li, Airborne spread of infectious agents in the indoor environment, Am. J. Infect. Control 44 (9) (2016) S102–S108.
[2] J. Gralton, E. Tovey, M.-L. McLaws, W.D. Rawlinson, The role of particle size in aerosolised pathogen transmission: a review, J. Infect. 62 (1) (2011) 1–13.
[3] L. Morawska, J. Cao, Airborne transmission of Sars-cov-2: the world should face the reality, Environ. Int. 139 (2020) 105730.
[4] S. Asadi, N. Bouvier, A.S. Wexler, W.D. Ristenpart, The coronavirus pandemic and aerosols: does Covid-19 transmit via expiratory particles?, Aerosol Sci. Technol. (2020) 635–638.
[5] Y. Li, C. Wu, G. Cao, D. Guan, C. Zhan, Transmission characteristics of respiratory droplets aerosol in indoor environment: an experimental study, Int. J. Environ. Health Res. (2021) 1–12.
[6] M.-R. Pendar, J.C. Páscoa, Numerical modeling of the distribution of virus carrying saliva droplets during sneeze and cough, Phys. Fluids 32 (8) (2020) 083305.
[7] Y. Zhou, S. Ji, Experimental and numerical study on the transport of droplet aerosols generated by occupants in a fever clinic, Build. Environ. 187 (2021) 107402.
[8] M. Jayaweera, H. Perera, B. Gunawardana, J. Manatunge, Transmission of Covid-19 virus by droplets and aerosols: a critical review on the unresolved dichotomy, Environ. Res. 188 (2020) 109819.
[9] D. Mirikar, S. Palanivel, V. Arumuru, Droplet fate, efficacy of face mask, and transmission of virus-laden droplets inside a conference room, Phys. Fluids 33 (6) (2021) 065108.
[10] V. Vuorinen, M. Aarnio, M. Alava, V. Alopaeus, N. Atanasova, M. Auvinen, N. Balasubramanian, H. Bordbar, P. Erästö, R. Grande, et al., Modelling aerosol transport and virus exposure with numerical simulations in relation to Sars-cov-2 transmission by inhalation indoors, Saf. Sci. 130 (2020) 104866.
[11] L. Zhang, Y. Li, Dispersion of coughed droplets in a fully-occupied high-speed rail cabin, Build. Environ. 47 (2012) 58–66.
[12] X. Yang, C. Ou, H. Yang, L. Liu, T. Song, M. Kang, H. Lin, J. Hang, Transmission of pathogen-laden expiratory droplets in a coach bus, J. Hazard. Mater. 397 (2020) 122609.
[13] T. Dbouk, D. Drikakis, On respiratory droplets and face masks, Phys. Fluids 32 (6) (2020) 063303.
[14] S. Verma, M. Dhanak, J. Frankenfield, Visualizing the effectiveness of face masks in obstructing respiratory jets, Phys. Fluids 32 (6) (2020) 061708.
[15] R. Bale, W.H. Wang, C.-G. Li, K. Onishi, K. Uchida, H. Fujimoto, R. Kurose, M. Tsubokura, A scalable framework for numerical simulation of combustion in internal combustion engines, in: Proceedings of the Platform for Advanced Scientific Computing Conference, 2020, pp. 1–10.
[16] R. Bale, C.-G. Li, M. Yamakawa, A. Iida, R. Kurose, M. Tsubokura, Simulation of droplet dispersion in Covid-19 type pandemics on fugaku, in: Proceedings of the Platform for Advanced Scientific Computing Conference, 2021, pp. 1–11.
[17] N. Zhu, D. Zhang, W. Wang, X. Li, B. Yang, J. Song, X. Zhao, B. Huang, W. Shi, R. Lu, et al., A novel coronavirus from patients with pneumonia in China, 2019, N. Engl. J. Med. (2020).
[18] R.G. Loudon, R.M. Roberts, Droplet expulsion from the respiratory tract, Am. Rev. Respir. Dis. 95 (3) (1967) 435–442.
[19] C.Y.H. Chao, M.P. Wan, L. Morawska, G.R. Johnson, Z. Ristovski, M. Hargreaves, K. Mengersen, S. Corbett, Y. Li, X. Xie, et al., Characterization of expiration air jets and droplet size distributions immediately at the mouth opening, J. Aerosol Sci. 40 (2) (2009) 122–133.
[20] S. Asadi, A.S. Wexler, C.D. Cappa, S. Barreda, N.M. Bouvier, W.D. Ristenpart, Aerosol emission and superemission during human speech increase with voice loudness, Sci. Rep. 9 (1) (2019) 1–10.
[21] X. Xie, Y. Li, H. Sun, L. Liu, Exhaled droplets due to talking and coughing, J. R. Soc. Interface 6 (suppl_6) (2009) S703–S714.
[22] J. Duguid, The size and the duration of air-carriage of respiratory droplets and droplet-nuclei, Epidemiol. Infect. 44 (6) (1946) 471–479.
[23] J.K. Gupta, C.-H. Lin, Q. Chen, Characterizing exhaled airflow from breathing and talking, Indoor Air 20 (1) (2010) 31–39.
[24] N. Jansson, R. Bale, K. Onishi, M. Tsubokura, Cube: a scalable framework for large-scale industrial simulations, Int. J. High Perform. Comput. Appl. 33 (4) (2019) 678–698, https://doi.org/10.1177/1094342018816377.
[25] K. Nakahashi, Building-cube method for flow problems with broadband characteristic length, in: Computational Fluid Dynamics 2002, Springer Berlin Heidelberg, 2003, pp. 77–81.
[26] P.L. Roe, Approximate Riemann solvers, parameter vectors, and difference schemes, J. Comput. Phys. 43 (2) (1981) 357–372.
[27] F.F. Grinstein, L.G. Margolin, W.J. Rider, Implicit Large Eddy Simulation, vol. 10, Cambridge University Press, Cambridge, 2007.
[28] C.-G. Li, M. Tsubokura, R. Bale, Framework for simulation of natural convection in practical applications, Int. Commun. Heat Mass Transf. 75 (2016) 52–58.
[29] H.O. Nilsson, Thermal comfort evaluation with virtual manikin methods, Build. Environ. 42 (12) (2007) 4000–4005.
[30] E.E. Broday, A.A. de Paula Xavier, R. de Oliveira, Comparative analysis of methods for determining the clothing surface temperature (tcl) in order to provide a balance between man and the environment, Int. J. Ind. Ergon. 57 (2017) 80–87.
[31] W. Ranz, W.R. Marshall, Evaporation from drops I, Chem. Eng. Prog. 48 (3) (1952) 141–146.
[32] W. Ranz, W.R. Marshall, Evaporation from drops II, Chem. Eng. Prog. 48 (3) (1952) 173–180.
[33] C.-G. Li, R. Bale, W. Wang, M. Tsubokura, A sharp interface immersed boundary method for thin-walled geometries in viscous compressible flows, Int. J. Mech. Sci. (2023) 108401.
[34] B. Binazzi, B. Lanini, R. Bianchi, I. Romagnoli, M. Nerini, F. Gigliotti, R. Duranti, J. Milic-Emili, G. Scano, Breathing pattern and kinematics in normal subjects during speech, singing and loud whispering, Acta Physiol. 186 (3) (2006) 233–246.
[35] R. Wölfel, V.M. Corman, W. Guggemos, M. Seilmaier, S. Zange, M.A. Müller, D. Niemeyer, T.C. Jones, P. Vollmar, C. Rothe, et al., Virological assessment of hospitalized patients with Covid-2019, Nature 581 (7809) (2020) 465–469.
[36] M.G. Prentiss, A. Chu, K.K. Berggren, Superspreading events without superspreaders: using high attack rate events to estimate n o for airborne transmission of Covid-19, MedRxiv (2020).
[37] W.F. Wells, Airborne Contagion and Air Hygiene: An Ecological Study of Droplet Infections, Harvard University Press, Cambridge, Mass., USA, 1955.
[38] T. Watanabe, T.A. Bartrand, M.H. Weir, T. Omura, C.N. Haas, Development of a dose-response model for Sars coronavirus, Risk Anal. 30 (7) (2010) 1129–1138.
[39] T. Watanabe, T.A. Bartrand, T. Omura, C.N. Haas, Dose-response assessment for influenza a virus based on data sets of infection with its live attenuated reassortants, Risk Anal. 32 (3) (2012) 555–565.
[40] R. Bale, A. Iida, M. Yamakawa, C. Li, M. Tsubokura, Quantifying the Covid19 infection risk due to droplet/aerosol inhalation, Sci. Rep. 12 (1) (2022) 1–15.
[41] J.L. Devore, Probability and Statistics for Engineering and the Sciences, Cengage Learning, 2015.